Solid-state NMR analysis of the dynamics of cofactors: comparison of Heliobacterial and purple bacterial reaction centers

Kim, Y.; Gräsing, D.; Alia, A.; Wiebeler, C.; Matysik, J.

THE JOURNAL OF PHYSICAL CHEMISTRY B
A JOURNAL OF THE AMERICAN CHEMICAL SOCIETY

pubs.acs.org/JPCB

Article

Solid-State NMR Analysis of the Dynamics of Cofactors: Comparison of Heliobacterial and Purple Bacterial Reaction Centers

Yunmi Kim, Daniel Gräsing, A. Alia, Christian Wiebeler, and Jörg Matysik*

Cite This: *J. Phys. Chem. B* 2024, 128, 11525−11545

Read Online

ACCESS | Metrics & More | Article Recommendations | Supporting Information

ABSTRACT: Photosynthetic reaction centers (RCs) serve as natural engines converting solar energy to chemical energy. Understanding the principles of efficient charge separation and light-induced electron transfer (ET) between the chlorophyll-type pigments might guide the synthesis for artificial photosynthetic systems. We present detailed insight into the dynamics at the atomic level using solid-state NMR techniques applied to the RCs of *Heliobacillus (Hb.) mobilis* (HbRCs) and the purple bacterium *Rhodobacter (R.) sphaeroides* (PbRCs). It is assumed that heliobacteria were among the first phototrophic organisms; therefore, their RC can be regarded as ancient. They are constructed homodimerically with perfect C_2 symmetry, enabling ET over both branches of cofactors. Modern RCs of *R. sphaeroides* wild-type (WT) have higher redox power and are functionally highly asymmetric. The dynamics of the cofactors in both RCs has been explored using nuclear hyperpolarization, induced by the solid-state photochemically induced dynamic nuclear polarization (photo-CIDNP) effect. Based on the individual incorporation of ^{13}C positions of the cofactors (through supplementation by ^{13}C-δ-aminolevulinic acid), photo-CIDNP magic-angle spinning (MAS) NMR experiments provide access to the local dynamics of the cofactors along the ET path over a broad range of time scales. Theoretical analysis of the dynamic deformation of these macrocycles is also discussed in terms of function. The dynamics observed in HbRCs appears to be correlated to ET. The cofactors in PbRC are significantly less dynamic than those in the HbRC. Relevance for efficiency and redox properties are discussed.

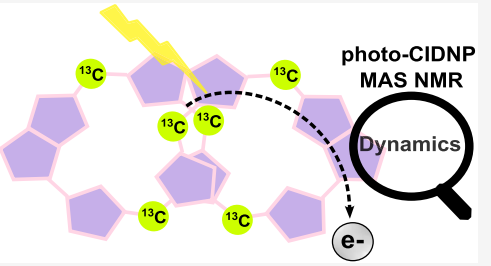

INTRODUCTION

Photosynthetic reaction centers (RCs) act as biological "solar cells", providing electric potential for cellular life.[1] RCs consist of protein−chromophore complexes designed to facilitate the conversion of light energy into chemical energy through electric charge separation across the cell membrane. These RCs, found in photosynthetic organisms, such as plants, algae, and bacteria, exhibit remarkably high quantum yields (almost unity) and efficiencies. Therefore, great effort has been made to understand the underlying mechanisms, also aiming at the design of artificial molecular photosynthetic systems[2,3] with strong potential in various fields such as medicine, optoelectronics, and solar fuels.[4]

The outstandingly high quantum yield is accomplished in RCs via a stepwise electron transfer (ET) over a chain of cofactors with virtually complete inhibition of electron back-transfer after light excitation. This unique property of RCs has been addressed by a number of experimental techniques, such as ultrafast time-resolved experiments[5−8] and studies of pigment fluctuations[9] and low-frequency vibrational modes.[10,11] Furthermore, light-driven structural changes during charge separation in the RCs have been investigated using X-ray structure analyses[12,13] as well as molecular dynamics (MD) simulations.[14−16] For interpretation, calculations were undertaken, exploring the link between ET and protein dynamics,[17] evaluating the electrostatic interaction energies of radical-pair states with their surroundings.[18] As described by Marcus theory, these ultrafast ET processes with efficiency close to unity are running kinetically and energetically in the inverted region, although dynamics is required to allow for electron−phonon coupling.[19,20] The exact interplay of "rigid" Marcus theory and necessary dynamics could potentially be a gap in our understanding of the role of active cofactors. An attempt to understand the role of these chromophores in ET should be based on the experimental measurements of these dynamics. In all natural photosynthetic RCs, these pigments are of the (bacterio)chlorophyll ((B)Chl) type,[21] whose macrocycles have particular opportunities for dynamics. (B)Chls exhibit great diversity among different photosynthetic organisms and show variability in photochemical and electrochemical properties while maintaining their basic function throughout Earth's history. As proposed by Shelnutt[22] and others,[23−25] conformations and conformational changes of the tetrapyrrole macrocycles as (B)Chls are associated with specific chemical properties. Experimental evidence for these proposals has been found by analyzing the displacement of low-

Received: June 19, 2024
Revised: October 21, 2024
Accepted: October 31, 2024
Published: November 8, 2024

https://doi.org/10.1021/acs.jpcb.4c04082
J. Phys. Chem. B 2024, 128, 11525−11545

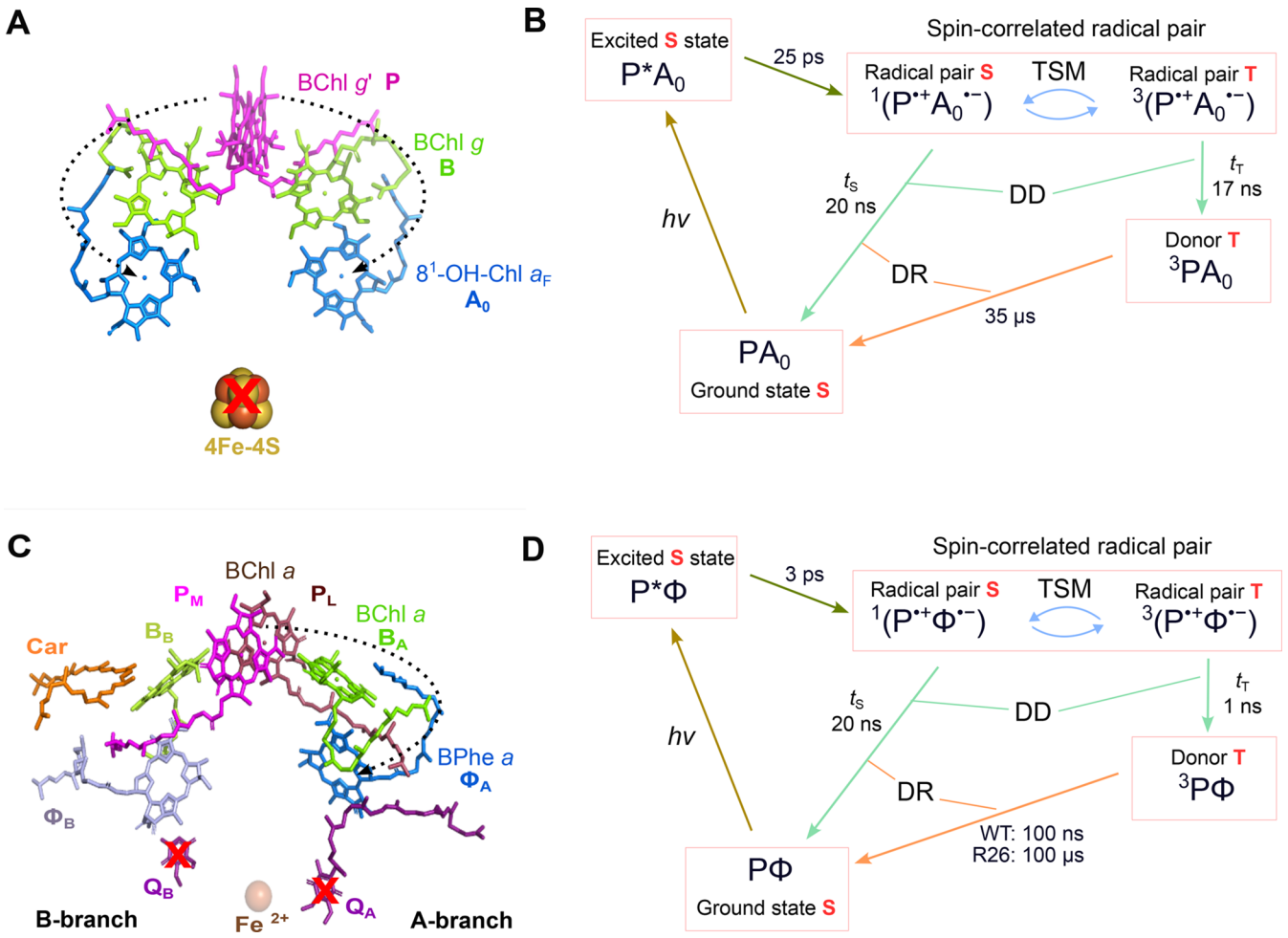

Figure 1. Cofactor arrangement of HbRC of *H. modesticaldum* [PDB: 5V8K] and ET pathway upon light excitation under the reduction of [4Fe-4S] (electron pathways are indicated with dashed black arrows) (A). The photocycle of HbRC with the involved solid-state photo-CIDNP mechanisms (B) is explained in the main text. Cofactor arrangement of PbRC of *R. sphaeroides* WT [PDB: 1M3X] (C). Upon light excitation, an electron is transferred from the special pair P to Φ_A, under quinone-depleted conditions (electron pathways are indicated with dashed black arrow). The photocycle of PbRCs of *R. sphaeroides* WT [PDB: 1M3X] with involved solid-state photo-CIDNP mechanisms (D) is explained in the main text. Prereduction or removal of quinones induces cyclic ET.

frequency vibrational modes using the normal-coordinate structural decomposition (NSD) method.[22]

Anoxygenic photosynthetic reaction centers (RCs) are believed to have appeared earlier in evolution than those involved in oxygenic photosynthesis.[26−28] The evolution of RCs is complex, involving divergence from a common ancestral reaction center that ultimately gave rise to the diverse RCs observed in modern photosynthetic organisms.[26,27] Hence, HbRCs are often considered among the most ancient RCs found in existing photosynthetic organisms, reflecting both their early divergence and structural simplicity.[28] These characteristics render HbRCs valuable models for studying the original photosynthetic photophysics and spin-dynamics. HbRCs have developed two fully symmetric branches for ET,[29−31] while the "modern", photosynthetic RCs of *Rhodobacter sphaeroides* WT are functionally highly asymmetric.[32−34] The X-ray structure of a HbRC from *Heliobacterium (H.) modesticaldum*, having a resolution of 2.2 Å[30] (see Figure 1A), is absolutely symmetrically arranged along the two ET branches, and the dimer of two bacteriochlorophyll *g*′ (BChl *g*′) molecules forming the special pair donor (P) shows perfect symmetry. Both, two 8¹-hydroxy-chlorophylls *a* with a farnesyl side chain (8¹-OH-Chl a_F) act as the primary acceptor A_0. In addition, an iron−sulfur [4Fe-4S] cluster serves as the terminal acceptor Fx.

Upon absorption of light by the HbRC, ET occurs from electronically excited primary donor P* to the primary electron acceptor A_0 within ∼25 ps at room temperature[35] (Figure 1B). Under reduction of terminal acceptor 4Fe-4S, a spin-correlated radical pair (SCRP) is formed between the radical cation state of special pair $P^{\bullet+}$ and the radical-anion state of primary acceptor $A_0^{\bullet-}$. This SCRP [$P^{\bullet+}A_0^{\bullet-}$] evolves between singlet and triplet states due to hyperfine interactions, electron Zeeman frequency difference. During this coherent spin evolution, nuclear hyperpolarization occurs via three-spin mixing (TSM).[36] Although recombination of the radical pair is allowed in its singlet state, it is forbidden in the triplet state, resulting in the formation of a donor triplet state (^{3}P). In HbRCs, the differential decay (DD) contribution[37,38] is negligible since the difference of lifetimes in these two decay channels is minimal (t_S = 20 ns *vs* t_T = 17 ns).[39,40] The lifetime of the donor triplet state (^{3}P) in HbRCs is (∼35 μs),[41−43] leading to the occurrence of the differential relaxation (DR) mechanism.[37] Consequently, hyperpolarized signals arising from donor or acceptor nuclei occur in the electronic ground state after recombination from either

https://doi.org/10.1021/acs.jpcb.4c04082
J. Phys. Chem. B 2024, 128, 11525−11545

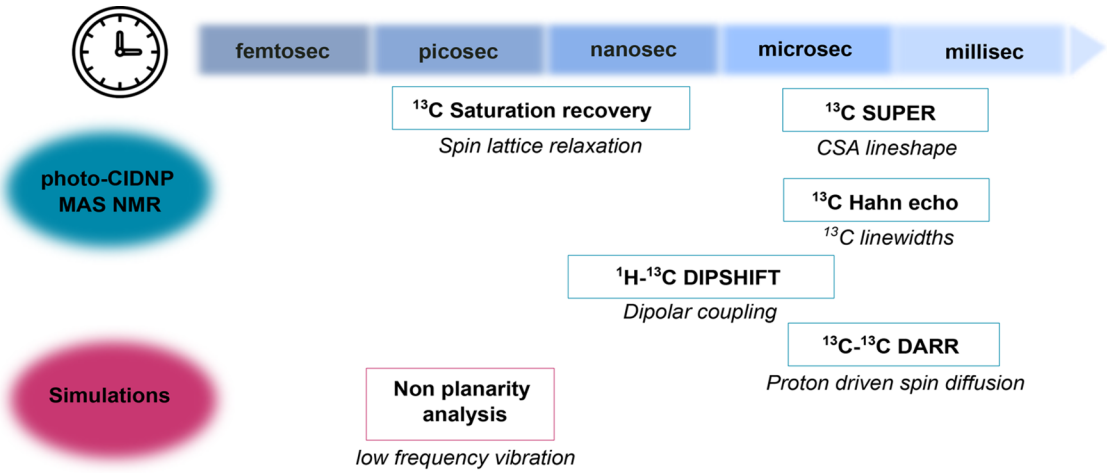

Figure 2. Overview of solid-state photo-CIDNP NMR experiments for probing internal dynamics of radical-forming cofactors across picoseconds to milliseconds time scales (for review see refs 59,60).

TSM and DR. Previous photo-CIDNP (photochemically induced dynamic nuclear nuclear polarization) MAS (magic-angle spinning) NMR studies on anaerobically treated *Hb. mobilis* (called *Braunstoff* in that study) demonstrate a strong magnetic field-dependent effect.[44,45]

The arrangement of cofactors and the kinetics of cyclic electron transport in PbRCs of *R. sphaeroides* WT under quinone-blocked conditions are depicted in Figure 1C,D. Two BChl *a* cofactors (P_L and P_M) form the special pair donor. Further cofactors are two accessory BChls (B_A and B_B), two bacteriopheophytins (BPhe Φ_A and Φ_B), two quinones (Q_A and Q_B), a non-heme iron, as well as a carotenoid (Car). The cofactors are arranged in two structurally rather symmetric branches, A and B. Despite their structural similarity, both branches exhibit a striking asymmetry in function. Only branch "A," referred to as the "active branch," facilitates ET, whereas branch "B" does not participate in the ET.[33] Upon absorption, within ∼3 ps,[46] ET occurs from excited special pair P* to the primary electron acceptor Φ_A, which is significantly faster than in the HbRC. Under quinone-depleted conditions, forward ET from Φ_A to Q_A is blocked, leading to the formation of an SCRP between the radical cation state of the special pair $P^{\bullet+}$ and the radical anion state of $\Phi_A^{\bullet-}$.[47] In the case of PbRCs of *R. sphaeroides* WT, the donor triplet state (^3P) is rapidly quenched by a nearby carotenoid cofactor acting as a triplet quencher (∼100 ns).[48] Hence, the DR mechanism is disregarded, and the TSM and DD mechanisms dominate.[49]

The formation of the SCRP between the primary donor and the acceptor upon light excitation opens the way to apply a special NMR technique, called photo-CIDNP MAS NMR. This approach is well suited for the selective study of the cofactors forming a SCRP within a large RC complex, as here, since the low selectivity and sensitivity caused by the unfavorable Boltzmann distribution is overcome.[48,50] If, as performed here, the RC to be studied is selectively ^{13}C isotopically enriched by adding the (B)Chl precursor *δ*-aminolevulinic acid (ALA), dynamics of the cofactors can be selectively probed against the background of the unlabeled proteins nuclei. Hence, the photo-CIDNP MAS NMR technique serves as a hyperpolarized NMR method for studying the ET machinery of photosynthetic RCs[45,49−54] and several flavoproteins[55−58] through the observation of the solid-state photo-CIDNP effect.[48,50] Upon illumination, an SCRP between the electron donor and the acceptor is created, and the electron spin polarization is transferred to nuclei by specific mechanisms such as the DD, DR, and TSM, resulting in dramatically enhanced signals detected with solid-state NMR. Furthermore, MAS NMR allows for chemical-shift resolution in solids as well as the study of a broad frequency range of internal motions. Therefore, in combination with various solid-state NMR methods, photo-CIDNP MAS NMR experiments enable the exploration of molecular dynamics over a wide frequency range.

Dynamic processes of molecules, modulating distances between atoms, their relative orientations, and bond geometries, cause fluctuations in NMR parameters, such as isotropic and anisotropic chemical shifts, quadrupolar couplings, dipolar couplings, and scalar couplings.[59] The dynamics window, ranging from picoseconds to seconds, can be investigated through various solid-state NMR methods. Exchange spectroscopy (EXSY)[61] and chemical-exchange saturation transfer (CEST),[62] based on isotropic chemical shift exchange, along with anisotropic interaction measurements by center-band-only detection of exchange (CODEX),[63] reflect slow exchange states ranging from milliseconds to seconds. These slow motions are beyond our current scope for studying the internal motion of (B)Chl cofactors. Line−shape analysis[64,65] probes the reorientation dynamics of micro- to millisecond time scale. Submicrosecond molecular motions can be explored using techniques such as separated-local field (SLF)[66,67] and dipolar chemical shift correlation experiments (DIPSHIFT),[68] which detect changes in the respective bond orientation.[69,70] Furthermore, internal dynamics from the pico- to microsecond range can be measured by T_1 relaxation time measurements.[71,72]

In this study, we investigate the local dynamics of selectively ^{13}C-labeled cofactors along the ET pathway in RCs of anaerobically treated *H. mobilis* and *R. sphaeroides* WT. Using solid-state NMR methodology, particularly photo-CIDNP MAS,[50,73] we analyze these dynamics at the atomic level on pico- to millisecond time scales. The photo-CIDNP MAS NMR experiments conducted in this study are illustrated in Figure 2. Essentially, we analyze the ^{13}C line width as a straightforward indicator of conformational dynamics. Specifically, we combine photo-CIDNP MAS NMR with DIPSHIFT, for probing $^1H-^{13}C$ dipolar coupling dynamics, SUPER for ^{13}C anisotropy line shape analysis, and ^{13}C T_1 relaxation time measurements. In addition, we apply photo-CIDNP dipolar-assisted rotational

https://doi.org/10.1021/acs.jpcb.4c04082
J. Phys. Chem. B 2024, 128, 11525−11545

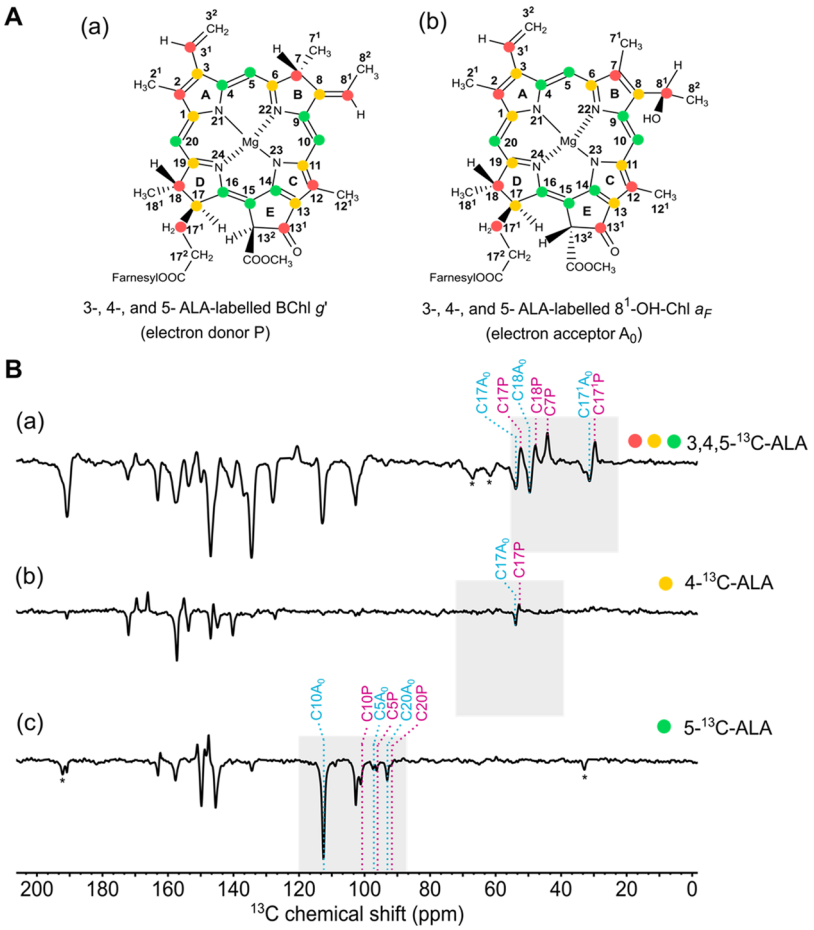

Figure 3. ^{13}C selective labeling pattern of [4-^{13}C]-, [5-^{13}C]-, and [3,4,5-^{13}C]-δ-ALA-labeled cofactors of HbRCs (A). 1D ^{13}C photo-CIDNP MAS NMR spectra of [4-^{13}C]-, [5-^{13}C]-, and [3,4,5-^{13}C]-δ-ALA-labeled membrane fragments of *Hb. mobilis* were recorded under continuous illumination at 488 nm (B). A cycle delay of 4 s was utilized at a field strength of 9.4 T, with a MAS frequency of 8 kHz for experiments conducted at 243 K. Signals from carbons carrying protons used for the DIPSHIFT experiment are underlaid in gray. Spinning sidebands are marked with asterisks.

resonance (DARR) MAS NMR for studying polarization buildup dynamics via spin diffusion based on a dipolar interaction. We also explored the temperature dependence of the dynamics of aliphatic carbons using photo-CIDNP DIPSHIFT MAS NMR, particularly examining changes near the glass transition of the protein matrix and the effects of the water hydration shell. Furthermore, we reconstruct low-frequency vibration dynamics of the cofactors in the electronic ground state and radical pair state to understand cofactor geometry upon forming the oxidation using *PorphyStruct* based on the Normal-coordinate Structural Decomposition (NSD) method.

EXPERIMENTAL METHODS

Sample Preparation. Cells of the *Hb. mobilis* strain DSMZ 6151 were used in this study. The cells were cultured in ATCC medium 1552[74] anaerobically at 37 °C under continuous illumination. For the selective isotope labeling of macrocyclic tetrapyrrole cofactors, cells were subcultured in medium 1552 supplemented with 1.5 mM [4-^{13}C]-δ-aminolevulinic acid (ALA), [5-^{13}C]-δ-ALA, or [3,4,5-^{13}C]-δ-ALA (Cortecnet, France), each serving as a precursor for the biosynthesis of B(Chl) cofactors. The ^{13}C labeling patterns of BChl and Chl are presented in Figure 3A, and were determined as previously described.[75,76] Grown cells were harvested by centrifugation at 15,000*g* and suspended in deoxygenated 20 mM Tris HCl buffer (pH 8.0) containing 10 mM sodium ascorbate. The cells were suspended in tris buffer and lysed by sonication for 30 min afterward, and the lysate was centrifuged at 20,000*g* for 15 min to remove the broken cells and debris. The resulting supernatant was ultracentrifuged at 200,000*g* for 4 h. The obtained pellet containing the membrane fragments was resuspended in 20 mM tris buffer (pH 8.0) with 0.02% sulfobetaine-12 (SB-12). The sample was reduced with 0.1 M sodium dithionite under a nitrogen gas flow and packed in an optically transparent 4 mm sapphire rotor for photo-CIDNP MAS NMR experiments.

Cultures of *R. sphaeroides* WT were grown anaerobically on synthetic Potnat medium as described earlier.[77] For selective ^{13}C isotope labeling of cofactors, the bacteria were grown in the presence of 1.0 mM [3-^{13}C], [4-^{13}C], or [5-^{13}C]-δ-ALA (Cambridge Isotope Laboratories, USA) essentially as described earlier.[77] and the labeling patterns are shown in Figure S2. The RCs were isolated as described by Shochat et al.[78] Quinones were removed by incubating the RCs at a concentration of 0.6 μM in 4% LDAO, 10 mM *o*-phenanthroline, and 10 mM Tris buffer (pH 8.0) containing 0.025% LDAO and 1 mM EDTA.[79] Approximately 15 mg of RC protein complex was packed in an optically transparent 4 mm sapphire rotor for photo-CIDNP MAS NMR experiments.

NMR Setup. All NMR experiments were conducted using a double-resonance-MAS probe on a Bruker AVANCE III spectrometer (Bruker-Biospin, Karlsruhe, Germany), operating at a proton Larmor frequency of 400.15 MHz (9.4 T).

https://doi.org/10.1021/acs.jpcb.4c04082
J. Phys. Chem. B 2024, 128, 11525−11545

Furthermore, DARR experiments were also performed by using a double-resonance MAS probe on a Bruker AVANCE NEO spectrometer (Bruker Biospin GmbH, Karlsruhe, Germany), operating at a proton Larmor frequency of 200.13 MHz (4.7 T). The temperature was calibrated using $Pb(NO_3)_2$[80] and the calibration curve is shown in Figure S1. All our photo-CIDNP MAS experiments were conducted on frozen samples, which minimizes the potential for RF heating effects.[81−83] The probe was equipped with a light fiber to illuminate the sample during the measurement. As an illumination source, a 488 nm 1-W continuous-wave laser (Genesis MX488-1000 STM OPS Laser-Diode System, Coherent Europe B.V., The Netherlands) was used. An optically transparent 4 mm sapphire rotor for 9.4 T and a 3.2 mm rotor for 4.7 T, respectively, were packed with membrane fragments and frozen in the dark at a slow spinning frequency of about 400 Hz to ensure a homogeneous sample distribution for stable spinning. All ^{13}C NMR spectra were referenced to the COOH response of solid L-tyrosine hydrochloride at 172.1 ppm.

The data was processed with Bruker Topspin 3.2 and further analyzed with MestReNova 14.1.0 (Mestrelab Research, Santiago de Compostella, Spain).

1D ^{13}C Photo-CIDNP MAS NMR. All NMR experiments were performed using Hahn-echo pulse sequence at a MAS frequency of 8 kHz, with a recycle delay of 4 s, and a temperature of 243 K. The $\pi/2$ ^{13}C pulses were applied at an RF field strength of 83 kHz. The 1D ^{13}C photo-CIDNP MAS NMR experiments were recorded with a Hahn-echo sequence with 1024 scans and 4 s relaxation delay. Swept-frequency two-pulse phase modulation (SW_f-TPPM) heteronuclear decoupling[84] was applied during acquisition, using an 85 kHz RF field and a 4.6 μs pulse duration.

Photo-CIDNP DIPSHIFT MAS NMR Experiment. The pseudo-2D 1Tr-recDIPSHIFT[85] experiments (as shown in the pulse sequence in Figure S5, CP (cross-polarization) block is replaced by $\pi/2$ pulse on ^{13}C channel) were conducted at a MAS frequency of 8 kHz, with a recycle delay of 4 s, and at temperatures of 243 and 215 K for HbRC of *Hb. mobilis*, 248 K for PbRC of *R. sphaeroides* WT. Four dummy scans were applied for each experiment. The $^1H-^1H$ homonuclear dipolar decoupling during the t_1 evolution period was accomplished by using the supercycled phase-modulated Lee−Goldburg (PMLG5)[86] scheme. Each PMLG5 block consisted of 10 pulses with the following phases: 339.22, 297.65, 256.08, 214.51, 172.94, 352.94, 34.51, 76.08, 117.65, and 159.22 (m5m shape in the Top-Spin 3.2 library). A PMLG5 RF amplitude of 82 kHz was used in the case of [3,4,5-^{13}C]-δ-ALA-labeled HbRC and [3-^{13}C]- and [4-^{13}C]-δ-ALA-labeled PbRCs, while a PMLG5 rf amplitude of 94 kHz was used in case of [5-^{13}C]-δ-ALA-labeled HbRCs and PbRC. The optimized PMLG5 pulse was 2.08 μs at an RF field of 82 kHz and 1.33 μs at an RF field of 94 kHz, respectively. Optimization was done by observing the J-splitting in adamantane powder using a PMLG5-decoupled CPMAS experiment.

Heteronuclear SW_f-TPPM decoupling[84] was employed during the acquisition with an RF field strength of 105 kHz. The spectral width was set to 41 kHz. The offset was set at 50 ppm for [5-^{13}C]-δ-ALA-labeled membrane fragments and at 105 ppm for [3,4,5-^{13}C]-δ-ALA-labeled fragments of *Hb. mobilis* and a total of 3072 scans were collected per each of the 17 t_1 increments. For the [3-^{13}C]-, [4-^{13}C]-, and [5-^{13}C]-δ-ALA-labeled PbRCs of *R. sphaeroides* WT, the offsets were set at 35, 52, and 105 ppm, respectively, and a total of 1024 scans were collected per each of the 17 t_1 increments. An exponential window function with 2 Hz line broadening was applied and the data was zero-filled to 8192 points prior to Fourier transformation. All 1Tr-recDIPSHIFT dephasing curves were fitted with SIMPSON[87] and the SIMPSON script used in this study is shown in Supporting Information (SI). A scaling factor for dipolar coupling was determined by running the 1Tr-recDIPSHIFT experiment on [u-^{13}C]-labeled L-Alanine and dividing the extracted dipolar couplings by the theoretical value of 23010 Hz (C−H distance of 1.095 Å,[88] determined scaling factors of 0.593 at 88 kHz RF field and 0.652 at 94 kHz RF field PMLG5 decoupling.

The order parameter S for the observed carbons is given by the ratio of the experimentally determined residual dipolar coupling and the dipolar coupling of the rigid limit, (S = residual dipolar coupling of sample/dipolar coupling of rigid limit). The rigid-limit values for CH and CH_2 groups were determined experimentally by measuring 1Tr-recDIPSHIFT for crystalline ^{13}C-enriched microcrystalline peptide fMLF (Formyl-Met-Leu-Phe), see Figure S6. For the fMLf sample, a cycle delay of 40 and 256 scans were employed for the 1Tr-recDIPSHIFT experiment. The order parameter S represents the average value derived from two SIMPSON fits based on two individual measurements. The errors in the order parameter S are derived from two independent experimental data sets and expressed as root-mean-square deviation (RMSD) divided by $\sqrt{2}$, reflecting experimental variation.

Photo-CIDNP SUPER MAS NMR Experiment. The pseudo-2D SUPER[89] experiments were performed on [4-^{13}C]- and [3,4,5-^{13}C]-δ-ALA-labeled HbRC of *Hb. mobilis* at a spinning frequency of 5 kHz, leading to an RF field of 60.60 kHz for CSA recoupling. The SUPER pulse sequence used for photo-CIDNP experiments described in previous study.[90] The γ-integral was set to one, with 1024 scans used per increment, and a total of 24 t_1-increments were recorded at 243 K. The spectral width was set to 32258 Hz, taking into account the scaling factor of 0.15547. The offset was placed at 110 ppm. Heteronuclear SW_f-TPPM decoupling[84] was used during the t_1 and t_2 acquisition. Frequency discrimination in all 2D experiments was achieved using the States-TPPI method.[91] The simulation of the CSA line shapes was carried out with SIMPSON[87] and the SIMPSON script used in this study is described in ref 90. In the SIMPSON simulation, three parameters were included in the input file: δ_{iso}, δ_{aniso}, and η. The δ_{iso} parameter was kept constant based on the chemical shift assignment, while δ_{aniso} and η were slightly varied to find the best fit. The five best fits for the powder pattern were selected, and the errors were derived from these fits, with uncertainties of ±1 ppm for δ_{aniso} and ±0.05 for η.

Photo-CIDNP Saturation Recovery Experiment. For the determination of the T_1 relaxation time, a saturation-recovery pulse scheme was used (satrect1 pulse program in the Top spin 3.2 library). Here, the magnetization is saturated by using a train of 80 equally spaced 90° pulses with a delay time of 20 ms between each pulse. SW_f-TPPM heteronuclear decoupling[84] with 85 kHz was used during the acquisition period. A temperature of 243 K was applied. Data were fitted using three-parameter exponential function, $B + F^*\exp(-x^*G)$.

2D $^{13}C-^{13}C$ Photo-CIDNP DARR MAS NMR. 2D $^{13}C-^{13}C$ photo-CIDNP DARR were performed on [3,4,5-^{13}C]-δ-ALA-labeled HbRC of *Hb. mobilis* with various mixing times: 2.5, 50, 200, and 500 ms. Throughout the mixing period, continuous-wave decoupling at ^1H was used to fulfill the rotary resonance

https://doi.org/10.1021/acs.jpcb.4c04082
J. Phys. Chem. B 2024, 128, 11525−11545

conditions $\nu_1 = n\nu_R$ (where $n = 1$ or 2)[92,93] with $n = +2$ at an RF field strength of 16 kHz. The total number of recorded scans was 512 with 120 increments in the indirect dimensions, and a relaxation delay time of 4 s was used for both magnetic fields. Swept-frequency two-pulse phase modulation (SW_f-TPPM) heteronuclear decoupling[84] was applied during acquisition, using an 85 kHz RF field and a 4.6 μs pulse duration. The light-induced 2D ^{13}C DARR spectrum was acquired over a period of approximately 3 days (58 h) at 243 K. Zero-filling to 4 K and an exponential apodization of 50 Hz was applied prior to Fourier transformation. Frequency discrimination was achieved using the States-TPPI method.[91]

Nonplanar Distortion Mode Analysis. The structures for the cofactors from HbRC of *H. modesticaldum* in their ground state and their radical state were taken from our previously reported calculations.[75] The structures for the cofactors of the RC of *R. sphaeroides* WT were extracted from the crystal structure [PDB: 1M3X]. Then, we followed the same computational protocol as in our previous study, i.e., employing Avogadro[94] to add missing hydrogen atoms and to truncate the longer side chain of each cofactor to a methyl group after the bond and utilizing Orca version 5.0.4[95] to perform geometry optimizations with the PBEh-3c method[96] for the electronic ground and radical states. The optimized structures, i.e., two cofactors from the optimized special pair and the acceptor, were then used in digital tool of *PorphyStruct*[97] based on the NSD method developed by Shelnutt et al.[98] The analysis utilized a nonmetal coordinated D_{4h} symmetric porphyrin as the reference molecule, the distortion is simulated by a linear combination of these orthonormal deformations using the lowest frequency normal coordinates of each symmetry type (minimal basis set). Exceptionally, for the acceptor Φ_A of PbRC of *R. sphaeroides* WT extended basis set was applied to reduce the deviation between simulation and experimental data.[97] The principle axes shown in Figure S14 are based on information extracted from the NMR calculation of our previous study.

RESULTS AND DISCUSSION

Generation of Hyperpolarized ^{13}C Signals of Donor and Acceptor Cofactors in both HbRCs and PbRCs as well as ^{13}C Line Width Analysis. The ^{13}C-selective labeling patterns of [4-^{13}C]-, [5-^{13}C]-, and [3,4,5-^{13}C]-δ-ALA-labeled cofactors of HbRCs are represented in Figure 3A and the corresponding 1D ^{13}C photo-CIDNP MAS NMR spectra obtained at 9.4 T are shown in Figure 3B. The solid-state photo-CIDNP effect in HbRCs is attributed to the TSM mechanism (negative, i.e., emmissive signals) for the electron acceptor A_0 and to a dominating DR mechanism (positive, i.e., enhanced absorptive signals) for the electron donor P.[75] The ^{13}C-selective labeling pattern of the cofactors in the PbRC of *R. sphaeroides* WT as well as photo-CIDNP 1D spectra obtained at 9.4 T are shown in Figure S2. The chemical shift assignments of cofactors and the solid-state photo-CIDNP mechanisms of the PbRC of *R. sphaeroides* WT have been well described in previous studies (for review,[99,100] see also Tables S2, S4 for the list of ^{13}C chemical shifts used in this study).

Alongside with the development of the theory, the solid-state photo-CIDNP effect has been developed into an analytical tool that enables the study of the local dynamics of cofactors.[50] The line width of the ^{13}C MAS NMR signals provides a source of information on conformational dynamics and local segmental motions, typically occurring on a micro- to millisecond time scale.[101] Increased inhomogeneous line-broadening reflects a larger distribution of different frozen conformational states, indicating slower molecular dynamics relative to the NMR time scale. We analyzed the ^{13}C line widths from [4-^{13}C]-δ-ALA-labeled membrane fragments of the RCs of *Hb. mobilis* and of *R. sphaeroides* WT (see Figures S3, S4 and Tables S1, S2). The average ^{13}C line width of the electron donor in the HbRC is significantly narrower than that of the acceptor (donor: 67.5 Hz (±14.1), acceptor: 81.2 Hz (±13.1)), indicating increased averaging of the conformational contributions due to faster motion. In the PbRC of *R. sphaeroides* WT, we observe a small asymmetry in the line width between P_L and P_M of the special pair, which might contribute to the functional asymmetry (P_L: 75.6 Hz (±13.3), P_M: 82.3 Hz (±14.9)). The average line width of ^{13}C of the acceptor is determined to be 85.3 Hz (±12.6). The narrower line width of ^{13}C nuclei of the donor in HbRC compared to the PbRC of *R. sphaeroides* WT suggests that the donor in the HbRC is likely more mobile than that in the modern RC.

Using [5-^{13}C]-δ-ALA-labeled membrane fragments of *Hb. mobilis*, also the temperature dependence of the line width has been probed. 1D ^{13}C photo-CIDNP MAS NMR spectra obtained at 215 and 243 K show differences in line-broadening (Figure S7). It is seen that, compared to the line width at 243 K, the line width at 215 K is significantly broadened. The signal at 112.6 ppm assigned to C10A_0, for example, is broadened from 48.6 to 57.4 Hz (full width at half height). Hence, molecular dynamics are slowed, and different conformations are frozen. It might be that the protein hydration shell becomes partially frozen, leading to broad chemical shift distributions.

Local Dynamics of Donor and Acceptor Cofactors by ^{13}C Photo-CIDNP DIPSHIFT MAS NMR. The DIPSHIFT MAS NMR method, designed to detect and quantify the motionally averaged heteronuclear ^{1}H−^{13}C dipolar coupling due to internal motion with the time scale of pico- to microsecond[67,85] is here combined with photo-CIDNP MAS NMR. The photo-CIDNP DIPSHIFT MAS NMR experiments are based on the 1Tr-recDIPSHIFT pulse sequence proposed by Iavnir-Dabora et al.[85] and the modified pulse sequence for photo-CIDNP experiments used in this study is shown in Figure S5. Specifically, aliphatic and methine carbons of cofactors in the HbRC, which allow for probing ^{1}H−^{13}C dipolar couplings, are marked with either pink (donor) or blue (acceptor) in Figure 3B. Due to the high intensity induced by the solid-state photo-CIDNP effect on the HbRCs, observation of the methine carbons C5, C10, and C20 as well as the aliphatic carbons C7, C17, C17^1, and C18 of donor and acceptor cofactors via photo-CIDNP DIPSHIFT MAS NMR experiments was found to be possible. The corresponding ^{1}H−^{13}C dephasing curves from two photo-CIDNP DIPSHIFT MAS NMR experiments were extracted and averaged to determine the dipolar coupling. The ^{1}H−^{13}C dephasing curves for the ^{1}H−^{13}C groups of electron donor and acceptor cofactors in HbRCs obtained at 243 K, respectively, are shown in Figure S10. For each curve, ^{1}H−^{13}C dipolar coupling was determined by SIMPSON simulation and the order parameters S were calculated, ranging from 0 (free isotropic motion) to 1 (rigid solid limit). For rigid-limit values assuming to be $S = 1$, rigid crystalline peptide fMLF (*N*-Formylmethionine-leucyl-phenylalanine) was taken and ^{1}H−^{13}C dipolar coupling for CH of Met α carbon was determined 24.4 kHz, see the results in Figure S6. The order parameters of the observed aliphatic and methine carbons of the electron donor and acceptor are determined by dividing the

https://doi.org/10.1021/acs.jpcb.4c04082
J. Phys. Chem. B 2024, 128, 11525−11545

experimental dipolar coupling value by the dipolar coupling value in the rigid limit. The experimentally obtained and fitted order parameters are shown in Table 1 and illustrated in Figure 4A,B.

Table 1. Order Parameters S at $^1H-^{13}C$ Positions in Electron Primary Donor (P), BChl g', and Acceptor (A_0), 8^1-OH-Chl a_F, in HbRC at 215 and 243 K, Respectively

carbon position	cofactor	chemical shift (ppm)	order parameter S^a at 215 K	order parameter S^a at 243 K
C5	P/BChl g'	97.2 (E)	0.74 ± 0.06	0.65 ± 0.08
	A_0/Chl a_F	96.2 (E)	0.79 ± 0.05	0.70 ± 0.13
C7	P/BChl g'	44.5 (A)	0.80 ± 0.04	0.79 ± 0.06
	A_0/Chl a_F			
C10	P/BChl g'	101.3 (E)	0.69 ± 0.04	0.75 ± 0.10
	A_0/Chl a_F	112.6 (E)	0.78 ± 0.01	0.83 ± 0.01
C17	P/BChl g'	52.8 (A)	0.76 ± 0.03	0.66 ± 0.11
	A_0/Chl a_F	53.9 (E)	0.89 ± 0.05	0.92 ± 0.06
$C17^1$	P/BChl g'	29.9 (A)	0.78 ± 0.02	0.68 ± 0.06
	A_0/Chl a_F	31.7 (E)	0.91 ± 0.06	1.00 ± 0.10
C18	P/BChl g'	48.0 (A)	0.94 ± 0.03	0.99 ± 0.05
	A_0/Chl a_F	49.8 (E)	0.86 ± 0.06	0.96 ± 0.04
C20	P/BChl g'	92.0 (E)	0.86 ± 0.12	0.69 ± 0.13
	A_0/Chl a_F	93.2 (E)	0.76 ± 0.04	0.81 ± 0.09

[a]Order parameters S are calculated by dividing the measured dipolar couplings by the values measured for the rigid crystalline peptide fMLf. The measured rigid-limit coupling strengths are D_{CH} = 24.4 kHz under PMLG decoupling. The errors are derived from two independent experimental data sets and are represented as RMSD divided by $\sqrt{2}$. Abbreviations: E (emmissive signal), A (absorptive signal).

For detailed analysis, we categorized the ^{13}C-labeled carbon positions into two groups, belonging to either the aromatic porphyrin macrocycle or the aliphatic farnesyl tail region. The extensive porphyrin π-system and the tail as a lipophilic anchor within the hydrophobic transmembrane proteins are well distinguished in dynamics, redox potential, and electronic absorption frequency.[102,103] The dynamics of C17, the connecting position of the farnesyl tail, can be significantly affected by the mechanical tension of the tail. Consequently, we classify this position as being part of the tail.

These data from HbRCs have several implications, as illustrated in Figure 4A,B: Order parameters of the donor compared to the acceptor experimentally obtained at 243 K are generally reduced. Specifically, the methine carbons C5P, C10P, and C20P of the donor have lower order parameters ranging from 0.65 to 0.75, indicating significantly higher dynamics, with C5P being the most mobile position. In contrast, C18P exhibits the highest order parameter, S = 0.99 among all carbon sites in the donor, indicating a high degree of rigidity. In the acceptor, a similar profile with local mobility at the methine carbons $C5A_0$, $C10A_0$, and $C20A_0$ is observed, however, slightly increased compared to that of the donor, while at $C18A_0$ the rigidity is similar to that of the donor. The highest local mobility on the donor is observed at C5P of the methine-bridge region between rings ***A*** and ***B*** where two donor cofactors are overlapping (see Figure 11A).

Furthermore, the starting point of the farnesyl tail exhibits a significant difference in the order parameters of the donor and acceptor carbons. Donor carbons C17P and $C17^1P$ show highly reduced order parameters of 0.66 and 0.68, respectively while those of the acceptor have values of 0.92 and 1.00. This indicates that the farnesyl tail of the donor side and its environment are exposed to notably more dynamics than the parts of the acceptor. One might assume that the porphyrin ring is less affected by the dynamics of the protein environment and that the donor side is more dynamic and less ordered than the acceptor site.

Although the kinetics of ET in photosynthesis is rather independent of the temperature range,[41,104,105] temperature does affect protein motion. In general, proteins undergo a phase transition concerning their dynamical properties in the temperature range of approximately 190−220 K.[106,107] Below this transition temperature, proteins adopt a glass-like state, where local vibrations dominate, whereas above this temperature, the dynamics relates more to the fluctuations between conformational substrates and global motion.[108,109] To study the temperature effect on the dynamics of a HbRC, we also performed the ^{13}C photo-CIDNP DIPSHIFT MAS NMR experiments at 215 K (Figure 4C−E).

The comparison of the order parameters of the electron donor obtained at two different temperatures, 215 and 243 K, is depicted in Figure 4D and the corresponding $^1H-^{13}C$ dephasing curve obtained at 215 K is shown in Figure S11. In the porphyrin region of the electron donor, the carbons such as C5P (from 0.65 at 243 K to 0.74 at 215 K) and C20P (from 0.69 to 0.86) show a slightly increased order parameter at the lower temperature. This trend is not only observed in the porphyrin but also occurs in the starting point of the farnesyl tail, as the order parameters of C17P (from 0.66 to 0.76) and $C17^1P$ (from 0.68 to 0.78) are slightly increased. The electron acceptor, however, exhibits a different trend (Figure 4E): Specifically, in the porphyrin, the carbons $C10A_0$ (from 0.83 to 0.78) and $C18A_0$ (from 0.96 to 0.86) show reduced order parameters at 215 K compared at 243 K. Moreover, at the beginning of the tail region, $C17A_0$ (from 0.92 to 0.89) and $C17^1A_0$ (from 1.00 to 0.91) demonstrate a decreased order parameter. The significant change in the beginning of the tail, at $C17^1A_0$, may be attributed to the reduced rigidity of the long hydrocarbon chain of farnesyl at low temperatures. This might be related to alterations in the order of the lipid environment at lower temperatures, which may influence the dynamics of the tail.[102] Hence, at the lower temperature, close to the glass transition, the entire acceptor site loses order, while at the donor site, the order increases upon cooling. Therefore, the contrast of local dynamics between the donor and the acceptor becomes less pronounced. Nevertheless, this dynamic behavior suggests that photosynthetic ET transfer, which is essentially temperature independent, is *not* controlled by this form of local dynamics. In particular, for a DIPSHIFT experiment, we expect the order parameter to be significantly affected at ambient temperatures by the surrounding protein matrix and the lipid environment.

To explore whether our observations on the evolutionary ancient HbRC are relevant for modern photosynthetic systems, too, we compare our data to ^{13}C photo-CIDNP DIPSHIFT MAS NMR data of the PbRC of *R. sphaeroides* WT using samples labeled with [3-^{13}C]-, [4-^{13}C]-, and [5-^{13}C]-δ-ALA. The order parameters of the $^1H-^{13}C$ sites of the special-pair donor cofactors, P_L and P_M, as well as of the acceptor Φ_A, are presented in Figure 5 and listed in Table S3. Additionally, the corresponding $^1H-^{13}C$ dephasing curves are shown in Figure S13. In general, all cofactors in the PbRC of *R. sphaeroides* WT are more rigid than those observed in HbRCs highlighting the uniformity in the order parameters (Figure 4). Among the carbons of all cofactors, C17 of Φ_A shows the lowest order

https://doi.org/10.1021/acs.jpcb.4c04082
J. Phys. Chem. B 2024, 128, 11525−11545

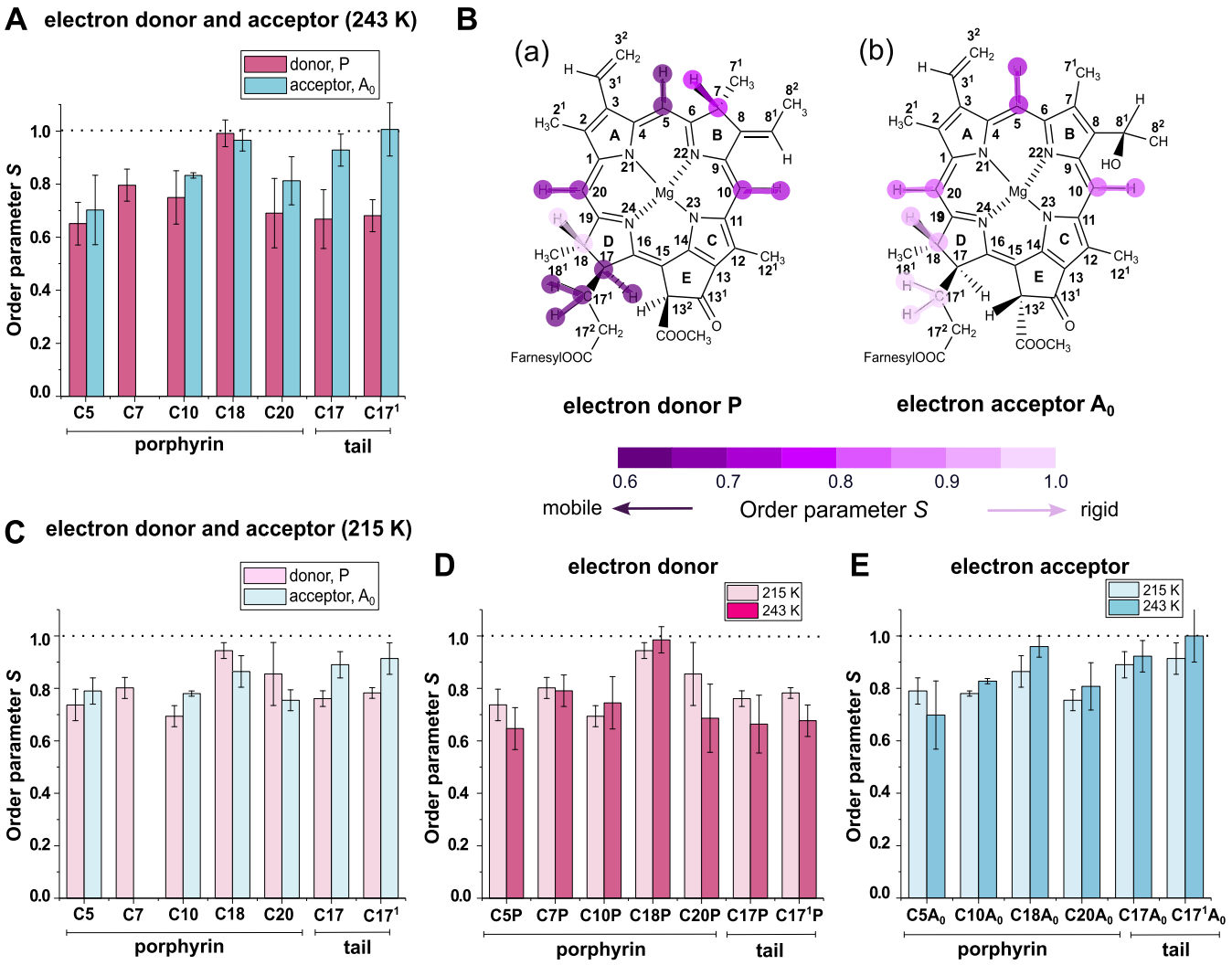

Figure 4. Comparison of order parameters S at $^{1}H-^{13}C$ sites of electron donor P and acceptor A_0, in HbRCs obtained experimentally at 243 K (A), along with an illustration of order parameter patterns on the cofactor structures, showing donor (a) and acceptor (b) in (B). The order parameters of the donor and acceptor were obtained experimentally at 215 K (C). The temperature dependence of the order parameter of electron donor (D) and electron acceptor (E).

parameter of 0.75, and several carbon sites, such as C5 and C20 of P_M, C8 of P_L, and C10 Φ_A exhibit relatively low order parameters, ranging from 0.80 to 0.84, indicating some degree of localized mobility.

According to Marcus theory, efficient ET systems operating on an ultrafast time scale, such as picoseconds, are generally expected to be rigid. Therefore, the observed "softness" of the HbRCs, as indicated by the order parameters, might be surprising, although it reflects slower dynamics than those associated with the ET process itself. However, the observed dynamics of CH bonds, spanning from ns to μs time scale, might play a role in facilitating efficient ET. Our data indicate that in the HbRC, the overlapping region in the special pair exhibits the highest mobility, while the donor cofactors show increased mobility. In PbRC, both the donor and acceptor appear to be stiffer than HbRCs, and there is no significant difference between the donor and acceptor sites.

Probing Reorientations of Electron Donor and Acceptor Cofactors by ^{13}C Photo-CIDNP SUPER MAS NMR. The CSA tensors allow for insight into electronic structure and dynamics in proteins on the time scale of micro- to milliseconds.[110,111] The SUPER MAS NMR experiment provides quasi-static powder patterns[89] with the information of principal values δ_{11}, δ_{22}, and δ_{33} of the CSA tensor. The parameters δ_{11}, indicating the tangential direction, and δ_{22}, the radial direction of the ring plane, while δ_{33} is aligned perpendicular to the molecular plane. The described orientation of the principal axes frame (PAF) is of consequence for the bond energy considerations of the sp^2-hybridized, mirror-symmetrical molecule discussed here. While the in-plane components mainly involve the π-electron system, the δ_{33} component is influenced by the circular shielding currents evoked by the σ bonding electrons. Thus, modifications of the two in-plane principal components of the quasi-static powder patterns, δ_{11} and δ_{22}, provide information on the chemical environment, such as electronic structure and hydrogen bonding.[112] As the origin of this functional symmetry break in the PbRC of *R. sphaeroides* WT, a rigid hydrogen bond between the acetyl group of P_L of the special pair and the His-L168 residue was proposed to cause the larger anisotropy.[90] The CSA span (Ω), defined as $\Omega = |\delta_{11} - \delta_{33}|$, provides information about the conformational dynamics of the investigated carbon nuclei, as it reflects the fluctuation of anisotropic interactions induced by the environment.[113]

https://doi.org/10.1021/acs.jpcb.4c04082
J. Phys. Chem. B 2024, 128, 11525−11545

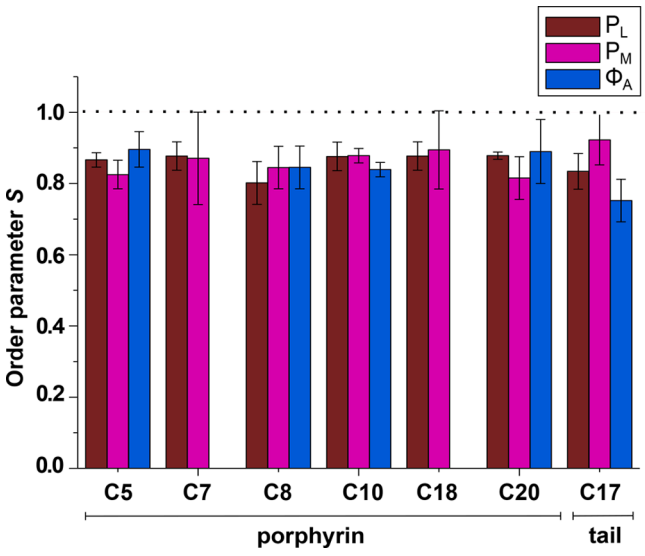

Figure 5. Order parameters S of $^{1}H-^{13}C$ sites of special pair P_L, P_M, and acceptor Φ_A in the PbRC of *R. sphaeroides* WT obtained at a temperature of 248 K.

In this section, we discuss the CSA span of the aromatic carbons on the (B)Chl cofactors. The calculated orientations of the principal axes (δ_{11}, δ_{22}, δ_{33}) on the molecular frame of C1, C4, C6, C9, C11, and C19 of the electron donor BChl g' and the acceptor 8^1-OH Chl a_F are shown in Figure S14, with similar profiles for all selected atoms. Therefore, the principal axes of C1, chosen as representatives of all selected atoms for both the electron donor and acceptor, are illustrated in Figure 6A. The comparison of experimental and simulated CSA spans for the selected aromatic carbons of the donor and acceptor is visualized in Figure 6B. The fitting parameters are listed in Table 2.

In general, both cofactors (donor: red, acceptor: blue) show similar forms of CSA at all selected carbon positions (see Figure 6B) of the donor and acceptor macrocycles. Only two carbon positions, C4 and C11, show distinct patterns between the electron donor and the acceptor. For C4, which is a part of ring *A*, the difference in $|\delta_{11} - \delta_{22}|$ is similar between the donor (C4P: 94.0 ppm) and acceptor ($C4A_0$: 92.7 ppm). However, there is a significant difference in the CSA span, with 122.0 ppm for the donor and 153.3 ppm for the acceptor, indicating environmental differences in both cofactors. This distinction may be attributed to the overlap of two electron donors, particularly in ring *A*, forming the special pair supermolecule with a common electronic structure. Conversely, for C11, there is a notable difference in $|\delta_{11} - \delta_{22}|$ (C11P: 121.3 ppm, $C11A_0$: 87.8 ppm), reflecting electronic structure differences between the two cofactors. We discuss this in detail with regard to the dynamics in the following.

Specifically, the CSA spans (see Figure 6B and Table 2) of C6 for the electron donor and acceptor are similar (C6P: 170.4 ppm; $C6A_0$, 167.8 ppm). However, C4 and C9 in the electron donor (C4P: 122 ppm, C9P: 134.5 ppm) are smaller than those in the electron acceptor ($C4A_0$: 153.3 ppm, $C9A_0$: 155.9 ppm), suggesting increased conformational mobility in the electron donor. Both atoms connect a pyrrole ring with a methine bridge and lie on opposite sides of the macrocycle. It might be that in the case of the donor, a "dynamic kink" can be found here. One could imagine that the donor cofactor shows dynamics similar to that of an open book: two hard covers connected by a hinge. In this region, the two electron donors overlap, here higher electron-spin density in the donor triplet has been observed in this region[75] (see also Figure 11D). However, the origin of the observed dynamics at C9 can be differently interpreted since the electronic environments, due to the interaction with the neighboring C8, differ between the donor (P) and acceptor (A_0).

The CSA span of carbons C1, C11, and C19 is substantially larger at the donor, indicating a greater conformational rigidity. Conversely, the acceptor in this region appears to be rather dynamic. The most mobile carbon in the acceptor is C11 (illustrated in Figure 6C(b)), correlating with the highest electron spin density region in the radical anion state. Since it is pointing toward the next electron acceptor (Fx),[75] both its charge density as well as its dynamics might be relevant for further ET. The 6 carbons C1, C4, C6, C9, C11, and C19 of both, donor and acceptor have a similar CSA span (mean: 157.2 ± 26.5 ppm for the donor, 153.9 ± 12.4 ppm for the acceptor). While the donor shows a large standard deviation of the CSA spans, the acceptor shows a smaller standard deviation of the CSA spans which might hint at uniformly distributed conformational dynamics of the carbon nuclei in the electron acceptor, as illustrated in Figure 6C(a,b).

Hence, in the overlapping region within a donor's special pair, potentially vital for regulating redox potential and electron pumping, we observe both high dynamics and spin density. This is also consistent with DIPSHIFT data on protonated carbons, as CSP on the methine bridge in the overlapping region of the donor was found to be the most mobile position. Furthermore, the location of the most mobile carbon in the electron acceptor coincides with the ET pathway leading to the terminal acceptor, providing further evidence of these connections.

^{13}C Spin–Lattice Relaxation Time by Photo-CIDNP MAS NMR Saturation Recovery. A further approach to probe the local dynamics of cofactors of RCs is based on the measurement of T_1 relaxation values.[59,70] T_1 relaxation, also called longitudinal relaxation, is sensitive to motions on the pico- to nanosecond time scales[59,60] caused by dipolar and CSA interaction exploring the fastest motions detectable by solid-state NMR experiments. Relaxation kinetics is magnetic field dependent.[60,114] In the present work, we limit ourselves to the results obtained at 9.4 T. The extracted T_1 values are presented in Figure 7 and saturation curves are shown in Figures S15–S17.

Figure 7 compiles the T_1 relaxation times of various carbons of the donor (red) and the acceptor (light blue) of HbRCs as well as that of the acceptor (dark blue) in the PbRCs of *R. sphaeroides* WT. Solely the three donor signals of C1, C6, and C19 of HbRCs provide sufficient peak area for determination of a T_1 value. The T_1 relaxation times of the few donor carbons of the HbRCs which were observed range between 0.9 and 1.9 s. In previous work,[75] we have shown that the solid-state photo-CIDNP effect of the donor carbons in HbRCs is due to the dominance of the DR over the TSM mechanism leading to positive (enhanced absorptive) signals from the donor and a very short T_1 time. Hence, T_1 values from donor carbons of HbRCs do not contain useful dynamic information.

Also, the T_1 relaxation times of the carbons of the acceptor of HbRCs are unusually short with the exception of $C16A_0$. A comparison with the T_1 data of the acceptor in the PbRC from the *R. sphaeroides* WT reveals a significant difference. Specifically, for the same carbon positions (C3, C6, C8, C11, C13, C17, and C19) in the [4-^{13}C]-δ-ALA-labeled RCs, HbRCs exhibit T_1 relaxation times ranging from 6.6 to 11.4 s, whereas the carbons in the acceptor of the PbRC from *R. sphaeroides* WT

https://doi.org/10.1021/acs.jpcb.4c04082
J. Phys. Chem. B 2024, 128, 11525–11545

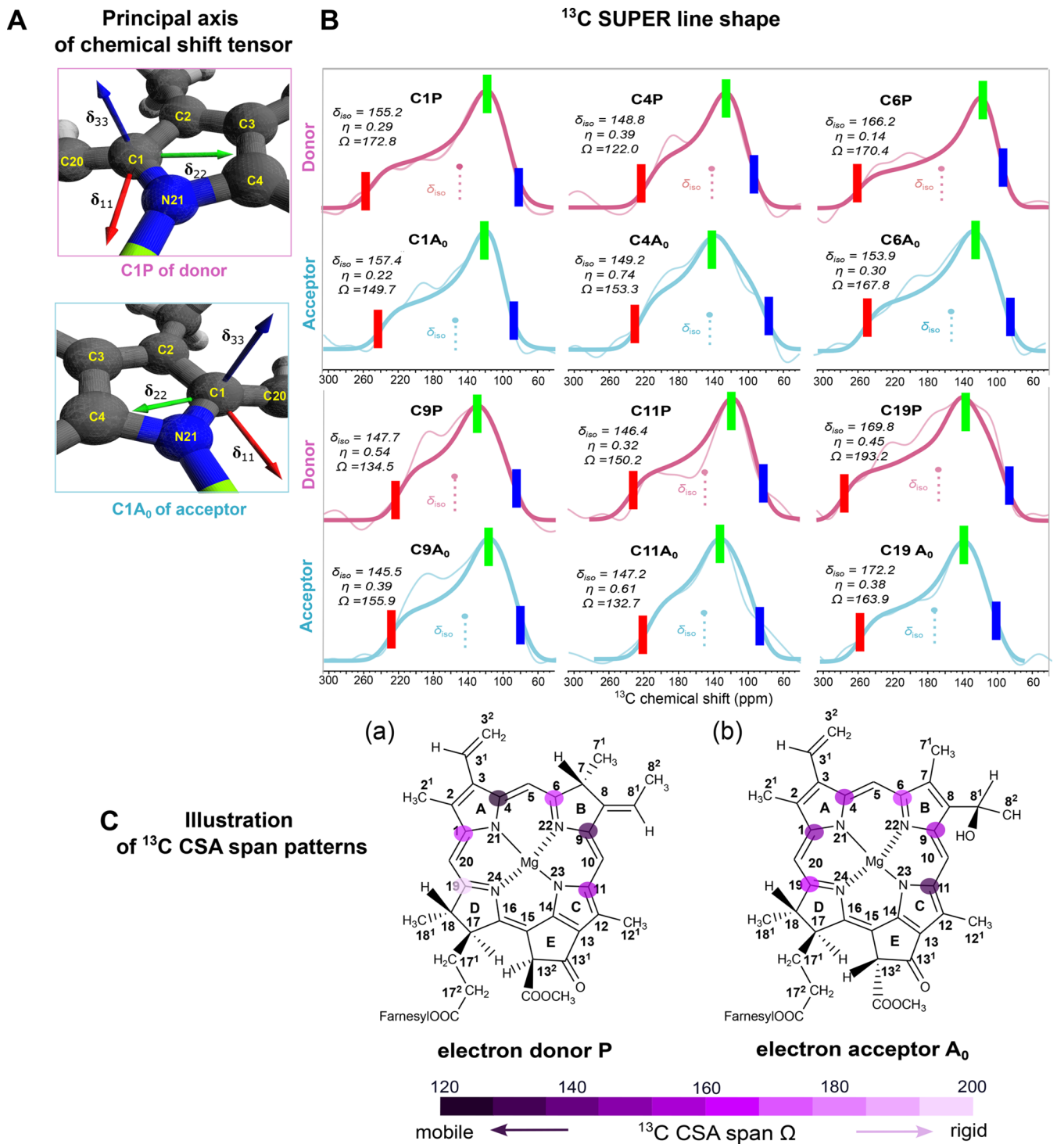

Figure 6. Representative orientations of the principal axes on the molecular frame of C1 for both the electron donor and the acceptor in a HbRC (A). Comparison of powder spectra of individual ^{13}C nuclei obtained as cross-sections from experimental photo-CIDNP SUPER MAS NMR spectra (thin line), acquired at a MAS frequency of 5 kHz, field strength of 9.4 T, and 243 K, with CSA powder patterns simulated using SIMPSON (thick line) (B). Figuratively assembled presentation of the dynamics of electron donor P (a) and acceptor A_0 (b) of HbRC based on of the ^{13}C CSA span (C). The data sets are provided in Table 2.

have T_1 values ranging from 9.1 to 15.6 s. The patterns of the T_1 relaxation time of the electron acceptor in both RCs are provided in Figure S21. This difference between the two RCs is remarkable since in both systems the hyperpolarized signals are arising from the electron acceptors and the enhancement is attributed to the TSM mechanisms.[75,47] The observed reduction of T_1 times of the acceptor carbons in HbRCs may be attributed to the presence of the reduced iron−sulfur cluster $[4Fe-4S]^{1+}$,[40,115] acting as a paramagnetic species in HbRC. This cluster is located within a distance of 11 Å (edge-to-edge) and 17 Å (center-to-center) from the electron acceptor. This proximity can induce reduced relaxation times due to the paramagnetic relaxation enhancement (PRE) effect. The PRE effect on the nuclear spin system is driven by the dipolar coupling between

https://doi.org/10.1021/acs.jpcb.4c04082
J. Phys. Chem. B 2024, 128, 11525−11545

Table 2. Line-Shape Parameters Obtained by Simulation Using SIMPSON of the Experimental ^{13}C CSA Spectra Obtained from the Photo-CIDNP SUPER MAS NMR Experiments[a]

	carbon no.	δ_{11}	δ_{22}	δ_{33}	δ_{iso}	span Ω	δ_{aniso}[b]	η[c]	$\lvert\delta_{11} - \delta_{22}\rvert$
electron donor	**C4 P**	220.8	126.8	98.8	148.8	122.0	72.0 ± 1.0	0.39 ± 0.05	94.0
	C6 P	274.7	119.5	104.4	166.2	170.4	108.5 ± 1.0	0.14 ± 0.05	155.2
	C9 P	223.7	130.2	89.2	147.7	134.5	76.0 ± 1.0	0.54 ± 0.05	93.5
	C11 P	236.9	115.6	86.7	146.4	150.2	90.5 ± 1.0	0.32 ± 0.05	121.3
	C19 P	281.8	139.0	88.6	169.8	193.2	112.0 ± 1.0	0.45 ± 0.05	142.8
	C1 P	260.2	117.9	87.5	155.2	172.8	105.0 ± 1.0	0.29 ± 0.05	142.3
electron acceptor	**C4 A_0**	231.2	138.5	77.9	149.2	153.3	82.0 ± 1.0	0.74 ± 0.05	92.7
	C6 A_0	252.9	123.7	85.1	153.9	167.8	99.0 ± 1.0	0.30 ± 0.05	129.2
	C9 A_0	237.5	117.4	81.6	145.5	155.9	92.0 ± 1.0	0.39 ± 0.05	120.1
	C11 A_0	220.7	132.9	88.0	147.2	132.7	73.5 ± 1.0	0.61 ± 0.05	87.8
	C19 A_0	269.2	142.1	105.3	172.2	163.9	96.0 ± 1.0	0.38 ± 0.05	127.1
	C1 A_0	250.4	121.1	100.7	157.4	149.7	93.0 ± 1.0	0.22 ± 0.05	129.3

[a]Signals are assigned to ^{13}C atoms of either the primary electron donor (P) or electron acceptor (A_0) cofactor. The principal values δ_{11}, δ_{22}, and δ_{33}, the isotropic chemical shift δ_{iso}, the reduced anisotropy δ_{aniso} and the CSA span Ω are given in ppm units. Furthermore, dimensionless value η is the asymmetry parameter. [b]$\delta_{aniso} = \lvert\delta_{11} - \delta_{iso}\rvert$, [c]Asymmetry parameter $\eta = \lvert\delta_{11} - \delta_{22}\rvert/\lvert\delta_{11} - \delta_{iso}\rvert$. The errors represent the uncertainties derived from the five best fits for the powder pattern, with ±1 ppm for δ_{aniso} and ±0.05 for η.

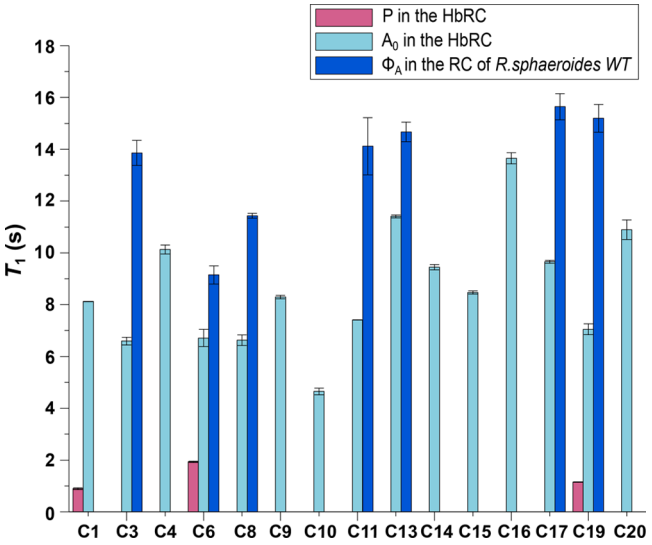

Figure 7. T_1 relaxation times of ^{13}C nuclei of the primary donor P (BChl g'), and acceptor A_0 (8^1-OH-Chl a_F) in the HbRCs of *Hb. mobilis*, and the acceptor Φ_A (BPhe *a*) in the PbRCs of *R. sphaeroides* WT. The data were obtained at 243 K under saturation recovery, continuous illumination at 488 nm, and a MAS frequency of 8 kHz at 9.4 T. The saturation curves are shown in Figures S15−S17.

the nuclear spin and the spin of paramagnetic species[116,117] and it can be induced at distances of up to about 24 Å.[118]

Hence, comparing T_1 relaxation times allows one to study spin dynamics, however, does not provide a useful approach to studying dynamics in the case of HbRCs due to the influence of the PRE effect.

Spin-Diffusion Kinetics Obtained in Photo-CIDNP $^{13}C-^{13}C$ DARR MAS NMR Experiments. Natural spin-diffusion, according to the concept of Bloembergen,[119] is defined as a polarization transfer between homonuclear spins driven by the dipolar interaction, which is a major mechanism for longitudinal relaxation processes in solids.[120,121] An effective spin diffusion rate reflects conformational local mobility and the relaxation effects.[122] In general, one would expect higher rates at lower fields since the increase of chemical-shift dispersion lowers spectral overlap. Hence, polarization transfer, as occurring in the $^{13}C-^{13}C$ DARR MAS NMR experiment can be used as a measure of local dynamics.[120] A previous photo-CIDNP MAS NMR study on the PbRC of *R. sphaeroides* WT discussed symmetry break in the local dynamics on the special pair of P_L and P_M by investigating the proton-driven $^{13}C-^{13}C$ spin diffusion profile.[123]

Ideally, the isotope labeling pattern of [3,4,5-^{13}C]-δ-ALA on HbRC provides a set of strong aromatic signals, inducing intensity enhancement in neighboring aliphatic carbons, with one partner being aromatic (producing hyperpolarization) and the other being aliphatic (receiving hyperpolarization). To this end, we selected the pairs $C13^1$/C14, C17P/$C17^1$, and C18/C19 on both the donor and acceptor cofactors. The dynamics probed, based on dipolar interaction, relies on motions occurring on the micro- to millisecond time scale. Here, we probe the buildup kinetics relying on spin diffusion by the cross-peak evolution in two-dimensional $^{13}C-^{13}C$ photo-CIDNP DARR MAS NMR experiments as a function of the variation of the mixing time from 2.5 to 500 ms (obtained DARR spectra are shown in Figures S19,S20).

The intensity buildup curves of the selected direct and two-bonded spin-pair correlations observed in [3,4,5-^{13}C]-δ-ALA-labeled membrane fragments at the magnetic fields of 4.7 and 9.4 T are shown in Figure 8. As discussed in our previous study,[75] the solid-state photo-CIDNP effect on HbRC is strongly dependent on the magnetic field, showing the dominance of the DR mechanism arising from the donor at 4.7 T, whereas the dominance of the TSM mechanism arises from the acceptor at 9.4 T (1D spectra obtained at 4.7 and 9.4 T are shown in Figure S18). At 4.7 T, due to the weaker TSM mechanism on the electron acceptor, only the single pair of $C13^1A_0$/$C14A_0$ is observed (Figure 8C). Although our data are limited, it appears that the kinetic profiles of the electron donor and acceptor are distinguished at different magnetic field strengths. The cross-peaks of the direct spin pairs of the donor, C17P/$C17^1$P and C18P/C19P, exhibit faster buildup at 4.7 T, with maximum intensity at 50 ms, while the cross-peak $C13^1$P/C14P builds up slower, reaching its maximum intensity at 200 ms (Figure 8A). This slower buildup behavior of $C13^1$P/C14P can be attributed to the extended distance in the pair with two bond distance. Indeed, the two direct spin pairs, C17P/$C17^1$P and C18P/C19P, exhibit almost identical profile. Hence, the difference in the profile seems to depend mainly on the spatial distance of the

https://doi.org/10.1021/acs.jpcb.4c04082
J. Phys. Chem. B 2024, 128, 11525−11545

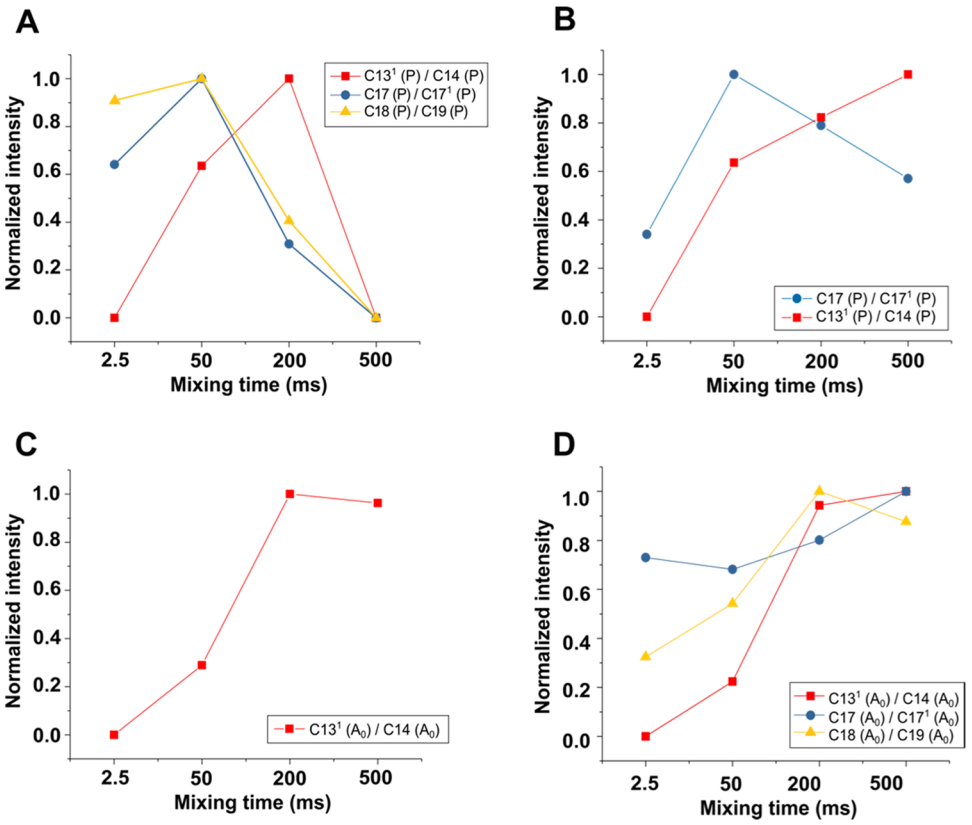

Figure 8. Buildup kinetics of cross-peak intensities of selected $^{13}C-^{13}C$ spin pairs. These curves are obtained from cross-peaks at various mixing times in photo-CIDNP $^{13}C-^{13}C$ DARR MAS NMR experiments obtained from [3,4,5-^{13}C]-*δ*-ALA-labeled membrane fragments of *Hb. mobilis* buildup curves of three selected nuclei spin pairs at the electron donor at 4.7 T (A), buildup curves of the same pairs at 9.4 T (B), buildup curves of the acceptor at 4.7 T (C), and buildup curves of the same pairs at 9.4 T (D). The light-induced signal intensity was normalized based on the peak area of the most intense peak. The two-dimensional $^{13}C-^{13}C$ photo-CIDNP DARR spectra are shown in Figures S19, S20.

two partner nuclei. At a higher magnetic field, at 9.4 T, the decay of C17P/C17¹P and C13¹P/C14P cross-peaks is slower than that at the lower magnetic field, 4.7 T, with the signal intensity remaining at 500 ms (see Figure 8B). At higher field, spectral overlap is smaller. Furthermore, the DR mechanism, based on the transient electronic paramagnetism of the donor during its molecular triplet state which enhances nuclear magnetic relaxation, is stronger at lower field.

Not surprisingly, the profile of the C13¹A_0/C14A_0 cross-peak of the acceptor, relying on the TSM is similar in both fields (Figure 8C,D). Additionally, we observe a different profile from the C17A_0/C17¹A_0 cross-peak, building up at a short mixing time of 2.5 ms (as shown in Figure 8D), which might be due to the rich proton environment enhancing proton-assisted spin diffusion.

In conclusion, we realized that the effects of spatial distance, spectral overlap, and relaxation rule these profiles; however, we were not able to extract conclusions concerning local dynamics.

Nonplanarity Analysis of Cofactors by Normal-Coordinate Structural Decomposition. Biological functions rely on molecular dynamics. As pointed out by Shelnutt,[22,98] porphyrin macrocycles show distortions correlating to regulate their biological function. Conformations of (B)Chls imposed by a conserved protein environment may also be relevant for controlling ET and redox properties in natural photosynthetic RCs.[124] As the principal geometric factor controlling their physicochemical properties, different forms of "nonplanarity" have been identified[125] which are linked to specific low-frequency out-of-plane vibrations occurring on the picosecond time scale. Here, we present our analysis on the deformation of electron donor and acceptor cofactors in both the electronic ground state and the charge-separated radical pair state of the two RCs.

The NSD method identifies the out-of-plane distortions observed in porphyrin geometries by identifying the low-frequency out-of-plane vibrational modes such as saddling (B_{2u}), doming (A_{2u}), ruffling (B_{1u}), and waving ($E_g(x)$) or ($E_g(y)$) as well as propelling (A_{1u}) (illustrated in Figure 9A). In the electronic ground state of the cofactors of the HbRC (Figure 9B,C), the total out-of-plane distortion (D_{oop}) of the primary electron donor (0.936 Å) exhibits a greater extent compared to the primary electron acceptor (0.533 Å). This trend, indicating that the donor is more mobile than the acceptor, is consistent with the DIPSHIFT data, as discussed in the previous section. Furthermore, ruffling (48%) and waving (*x*-direction) (22%) are predominant conformations of the electron donor, while saddling (44%) and doming (22%) are prominent at the electron acceptor. Although redox potential is strongly modulated by the electrostatic effect of surrounding protein residues,[126] a recent study has demonstrated that the redox potential of heme models decreases as a function of displacement along the ruffling mode, while the saddling mode elevates the redox potential.[24,25] Thus, the increase in redox potential from the electron donor (+0.225 V)[127,128] to the primary acceptor (−0.85 V)[128,40] is related to the deformation of cofactors within the protein environment.[75]

Another notable result relates to the size of the cavity formed by the square between the four pyrrole nitrogens, which is also

https://doi.org/10.1021/acs.jpcb.4c04082
J. Phys. Chem. B 2024, 128, 11525−11545

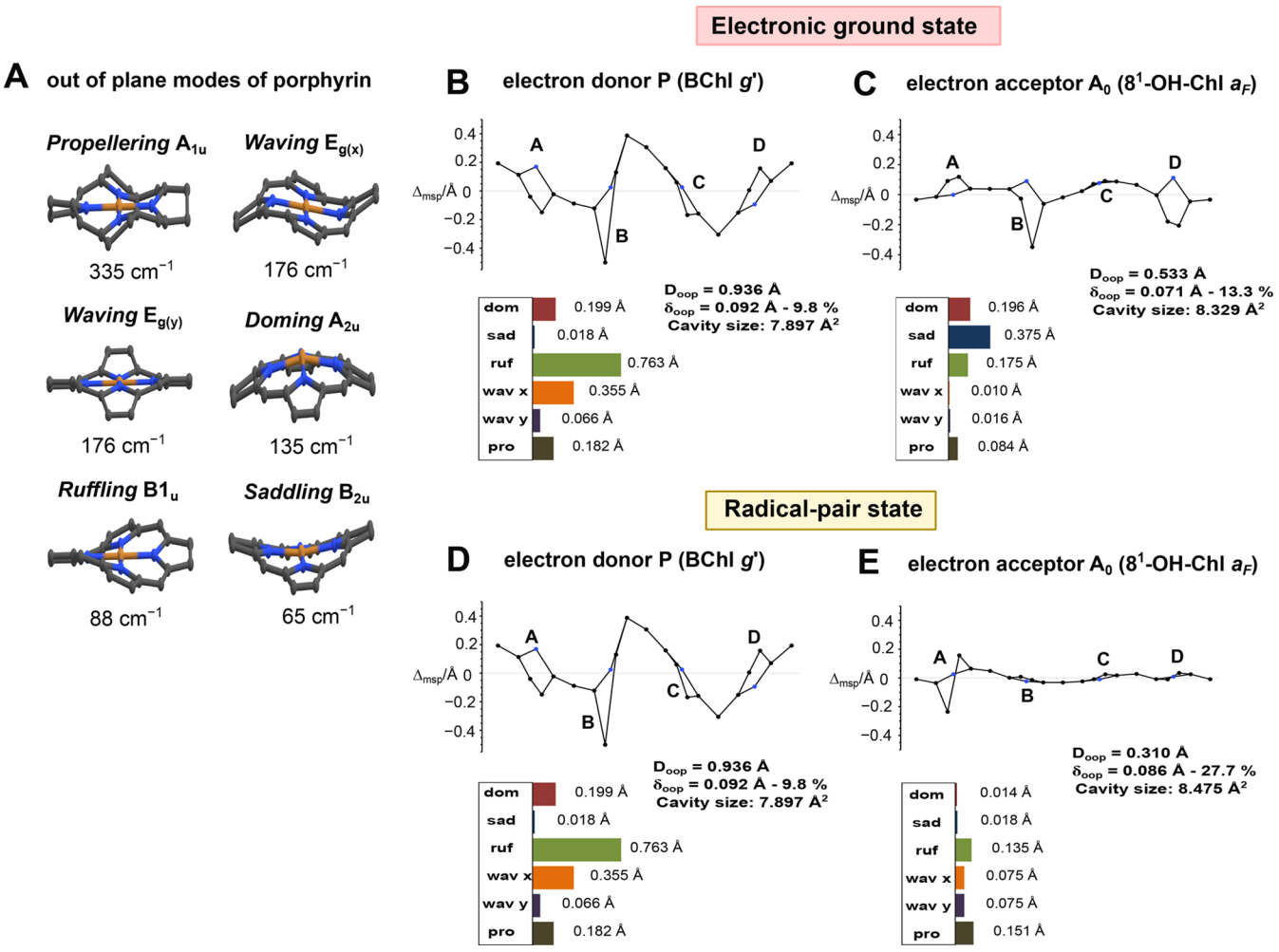

Figure 9. Overview of the low-frequency out-of-plane vibrational modes of the porphyrin rings.[97] (A) The vibrational analysis results of the cofactors in the HbRC obtained using *PorphyStruct*. The electron donor BChl *g*′ (B) and the acceptor 8¹-OH-Chl a_F (C) cofactors in the electronic ground state as well as the donor BChl *g*′ (D) and the acceptor 8¹-OH-Chl a_F (E) cofactors in the radical-pair state. The top row displays the molecular structure and linear representation of nonplanar distortions, while the bottom row presents a color-coded bar plot indicating the contribution of the different low-frequency out-of-plane modes.

obtained by the NSD calculations. For all six types of out-of-plane distortion, the distance between the four central nitrogen atoms inevitably changes. In particular, the size of the cavity increases upon doming distortion, while the size of the cavity shrinks with the ruffing distortion.[129] The size of the cavities in the primary acceptor (8.329 Å²) of the HbRC exceeds that of the primary donor (7.897 Å²). Also, the increase in the cavity size has been related to an increase in redox potential.[129]

From both cofactors, also the radical-pair state of HbRC has been analyzed by NSD calculations (Figure 9D,E). The electron donor remains structurally unchanged after oxidation compared to the electronic ground state. According to Marcus, a low activation energy is indeed a prerequisite for efficient ET.[19,20] The electron acceptor, however, becomes flatter after reduction with the exception of pyrrole ring *A*, which reduces the contribution of the saddle mode in particular. The contribution of the ruffing mode remains similar so that the cavity size remains constant. The significant structural change of the electron acceptor upon radical-pair formation might prevent back transfer by causing a high reorganization energy allowing for maintaining high efficiency.

To explore the evolutionary implications for bacterial photosynthetic systems, we compare cofactor deformations of the HbRC with those of the PbRC of *R. sphaeroides* WT. The results depict the deformation of the three cofactors: P_L and P_M of the donor special pair, and the electron acceptor Φ_A (Figure 10).

While in HbRCs, both halves of the RC are identical and the ET runs symmetrically over both branches of cofactors, in the RC of *R. sphaeroides*, the two halves are structurally and electronically well distinguished,[130] and the ET occurs selectively via the A branch.[131] This functional symmetry break is also expressed in differences in structural deformation and vibrational motions between P_L and P_M (Figure 10A,B). The contribution of low-frequency modes is ruled for P_L in the electronic ground state by ruffling, while doming dominates the motion of P_M. Interestingly, the total out-of-plane distortion (D_{oop}) between these two donors, P_L and P_M, remains constant.

Also in the radical-cation state of the special pair donor, the electronic structure is asymmetric: the distribution of spin density in the special pair in the radical-cation state was determined to be 2:1 $P_L^{\bullet+}/P_M^{\bullet+}$ by ^{1}H ENDOR[132] and ^{13}C photo-CIDNP MAS NMR studies.[133] According to the NSD analysis (Figure 10D,E), both donor cofactors undergo small structural and dynamic changes. Specifically, the total distortion D_{oop} of P_M increases. Surprisingly, it appears as if the pattern of

https://doi.org/10.1021/acs.jpcb.4c04082
J. Phys. Chem. B 2024, 128, 11525−11545

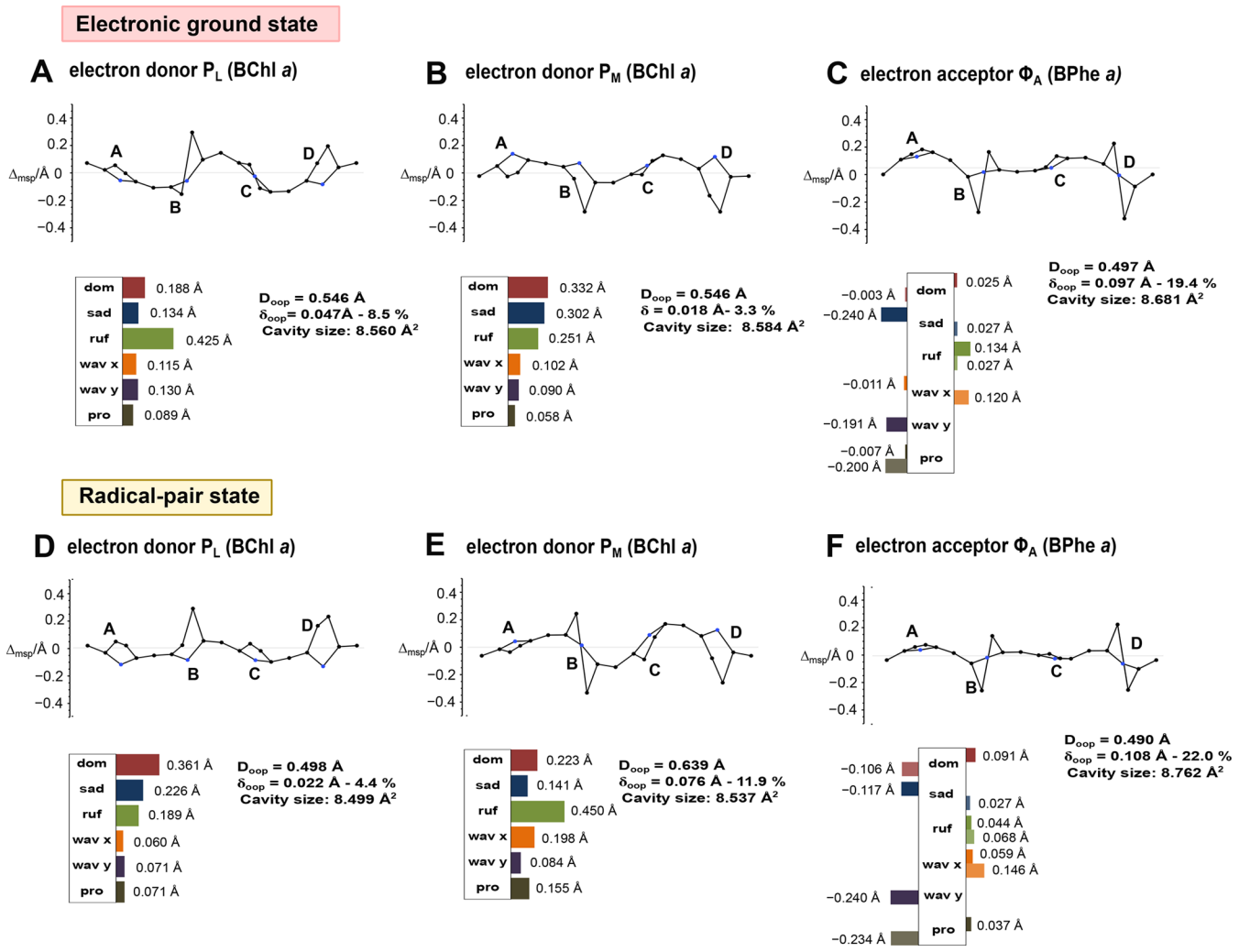

Figure 10. Overview of the low-frequency out-of-plane vibrational modes of the porphyrin rings of the three cofactors of the PbRC of *R. sphaeroides* WT analyzed by NSD: the donor special pair of P_L (BChl *a*) (A) and P_M (BChl *a*) (B) as well as the acceptor Φ_A (BPhe *a*) (C) cofactors along the A branch in the electronic ground state, and of the donor special pair of P_L (D) and P_M (E) as well as of the acceptor Φ_A (F) cofactors in the radical-pair state. The top row displays a linear representation of nonplanar distortions of the macrocycle, while the bottom row presents a color-coded bar plot indicating the contributions of the low-frequency modes.

low-frequency oscillations between the two cofactors is reversed as a result of the oxidation. One might speculate whether these observations are related to the functional symmetry break, i.e., the asymmetric ET. In any case, the very fast light-induced ET in PbRCs of *R. sphaeroides* WT, from the special pair to the BPhe *a* cofactor (~3 ps),[46] has been reported to be coupled to coherencies.[134−136] The ET in HbRCs is significantly slower (~25 ps),[35] and, until now, no coupling to vibrational modes has been reported. It might be that an acceleration of the ET, and thus also the improvement of quantum yield, by enhanced electron−phonon coupling is a later adaptation in the biological evolution of photosynthetic systems due to specialization of the two sides of the RCs.

The total distortion dynamics of electron acceptor Φ_A in the PbRC of *R. sphaeroides* WT is limited in both, the electronic ground state (0.497 Å) and the radical-pair state (0.490 Å) (Figure 10C,F). Moreover, the changes in structure and vibrational dynamics are very minor. That is in contrast to the substantial changes observed in the electron acceptor of HbRC (Figure 9C,E). This difference might reflect the construction differences between Type-I and Type-II RCs. In Type-I RCs the acceptor side is structurally fixed, i.e., no molecule undergoes chemical exchange with the environment. As a functional "molecular diode", suppressing back-ET, the electron acceptor A_0 has been identified. In Type-II RCs, the reduced quinone molecules exchange with the quinone pool of the membrane. Although light-induced structural changes of BPhe *a*[137,138] and Q_A[139,140] are reported, the final electron acceptor Q_B[12,141,142] undergoes dramatic changes which are called "Kleinfeld effect".

In any case, in both types of RCs, the acceptor site appears to be less dynamic than the donor site. Moreover, the dominant low-frequency vibrational mode is saddling in the electronic ground-state of both electron acceptors, while ruffling dominates in the electronic ground-state of the donor cofactors. It appears that the conserved dynamics observed in these two photosynthetic RCs are linked to their respective functions of oxidation for the donor and reduction for the acceptor.[124,125] It also appears that evolution allowed the flattening of the overall geometry of the cofactors in their electronic ground state. One might assume that flatting of the porphyrin is related to tightening of the positively charged nuclear skeleton, allowing

https://doi.org/10.1021/acs.jpcb.4c04082
J. Phys. Chem. B 2024, 128, 11525−11545

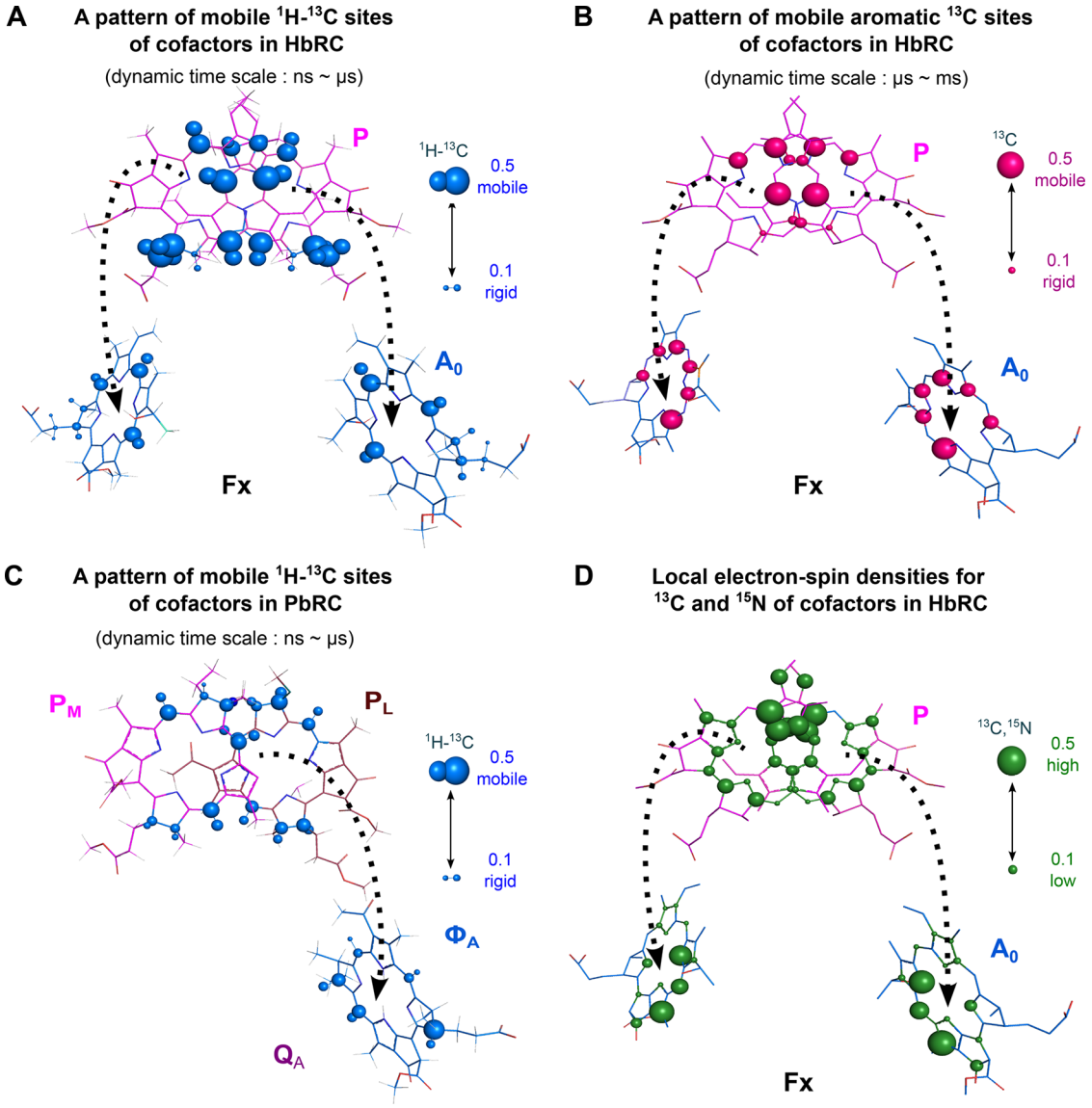

Figure 11. Pattern of mobile ^{1}H−^{13}C sites of cofactors in the HbRC based on the order parameter *S* obtained from photo-CIDNP DIPSHIFT MAS NMR experiments at 243 K (A). A pattern of mobile ^{13}C sites of cofactors in the HbRC based on ^{13}C CSA span obtained from photo-CIDNP SUPER MAS NMR experiments at 243 K (B). Pattern of mobile ^{1}H−^{13}C sites of cofactors in the PbRC based on the order parameter *S* obtained from photo-CIDNP DIPSHIFT MAS NMR experiments at 248 K (C). Map depicting the local spin density distribution for ^{13}C and ^{15}N of the donor in the triplet state and the acceptor in the radical anion state in the HbRC was obtained from ^{13}C photo-CIDNP MAS NMR experiments at 243 K and modified from ref 75 (D). The sphere size represents scaled values based on the order parameter *S* (blue) and the CSA span (pink), electron spin densities (green), respectively. Electron pathways are indicated with dashed black arrows and cofactor geometries were taken from the PDB: 5V8K for HbRC and 1M3X for PbRC.

the same electronic architectures to reach a higher redox potential.

CONCLUSIONS

Based on ^{13}C photo-CIDNP MAS NMR methodology and theoretical analysis, the dynamics of the (B)Chl cofactors acting in photosynthetic ET have been probed at a broad range of time scales. In particular, we compare ancient HbRCs, photosynthetic pioneers, with the more advanced PbRC of *R. sphaeroides* WT, a precursor of photosystem II. Our attempts to extract dynamic information from T_1 relaxation and spin-diffusion data had limited success but backed our conceptual understanding of the mechanism of the solid-state photo-CIDNP effect. Therefore, our dynamics analysis of the cofactor relies on ^{13}C line widths, DIPSHIFT, and SUPER photo-CIDNP MAS NMR, which may indirectly report on the tuning of cofactor dynamics for efficient ET, while the theoretical NSD analysis can directly reflect the initial ET process. Our main findings are therefore

- In HbRCs, the donor region is more mobile than the acceptor region as probed by both DIPSHIFT (dynamics on the nano- to microsecond time scale) and SUPER (micro- to millisecond time scale) experiments (Figures 11A,B and S22). These methods detect the molecular dynamics in the same regions: in the overlapping area of the donor cofactors as well as in the acceptor region toward the iron−sulfur cluster Fx. In previous work, these regions were also detected to carry enhanced electron spin density in the radical-pair state (Figure 11D).[75]

https://doi.org/10.1021/acs.jpcb.4c04082
J. Phys. Chem. B 2024, 128, 11525−11545

- In PbRCs of *R. sphaeroides* WT, the donor and acceptor are more rigid (see Figure 11C) than in the HbRC (Figure 11A). This is also consistent with the narrower line width of the donor signals of the HbRC, which reflects conformational states averaged by dynamics, compared to those of the PbRC of *R. sphaeroides* WT.
- In PbRCs, the DIPSHIFT data show no major difference in the dynamics of donor and acceptor sites; both are stiffer compared to those in HbRC. Nevertheless, similar to the donor in HbRCs, the strongest dynamics in the donor of PbRCs are observed in the overlap region of the cofactors, particularly at C5.
- The theoretical NSD analysis, which pertains to the picosecond time scale directly relevant to initial ET, shows that in both types of photosynthetic RCs in their electronic ground state, the donor exhibits more dynamic behavior than the acceptor. In particular, the dominant vibrational mode of the donor is ruffling, while saddling predominates in the acceptor, which is consistent with their function.
- The slower ET rates from donor to acceptor (~25 ps)[35] in the HbRC compared to those in the PbRCs of *R. sphaeroides* WT (~3 ps),[46] which may also be associated with lower efficiency, could be related to the overall dynamics of the cofactors and the protein matrix. Thus, during evolution, nature has succeeded in enhancing the interplay of rigidity and electron−phonon coupling.
- One might speculate that the degree of global protein mobility does depend on the number of charged amino acid residues in the protein matrix, which could cause salt-like rigidity by charged architecture, however, our analysis based on FASTA data[30,143] shows that both RCs contain about 11% charged amino acids (data not shown).
- It also has been reported that the number of hydrogen bonds of the donor dimer to the protein matrix strongly affects its redox potential and ET rates: An increasing number of hydrogen bonds causes a higher redox potential and faster ET rates.[144] Indeed, the mobile donor of HbRC has no hydrogen bonds with its surroundings,[30] whereas rigid special pair of *R. sphaeroides* WT has one hydrogen bond, leading to a higher redox potential and faster ET rates.
- In the case of HbRC, the formation of the radical pair leads to considerable structural changes in the acceptor, which might hinder retransfer due to a high activation energy This "diode" function could correspond to the Kleinfeld effect in PbRCs.
- The stiffer RCs might have enabled a higher oxidative power (e.g., redox potential of donor: +0.225 V in HbRCs,[127,128] +0.5 V in the PbRC[145,146]). One might assume, comparable to a mechanical spring, that higher stiffness contributes to a spatial confinement of structural deformations (e.g., by Coulomb forces), while soft environments escape the buildup of high forces by structural rearrangements.

■ ASSOCIATED CONTENT

Supporting Information

The Supporting Information is available free of charge at https://pubs.acs.org/doi/10.1021/acs.jpcb.4c04082.

Additional experimental details, including the pulse sequence and SIMPSON script, as well as further results, including NMR spectra and the figures referenced in the text, are provided in Figures S1−S22 and Tables S1−S3 (PDF)

■ AUTHOR INFORMATION

Corresponding Author

Jörg Matysik − *Institut für Analytische Chemie, Universität Leipzig, D-04103 Leipzig, Germany;* orcid.org/0000-0002-7800-7443; Phone: +49-341-9736112; Email: joerg.matysik@uni-leipzig.de; Fax: +49-341-9736115

Authors

Yunmi Kim − *Institut für Analytische Chemie, Universität Leipzig, D-04103 Leipzig, Germany*

Daniel Gräsing − *Institut für Analytische Chemie, Universität Leipzig, D-04103 Leipzig, Germany*

A. Alia − *Institut für Medizinische Physik und Biophysik, Universität Leipzig, D-04107 Leipzig, Germany; Leiden Institute of Chemistry, Leiden University, 2301 RA Leiden, The Netherlands*

Christian Wiebeler − *Institut für Analytische Chemie, Universität Leipzig, D-04103 Leipzig, Germany; Institut für Physik, Universität Augsburg, D-86159 Augsburg, Germany;* orcid.org/0000-0003-1286-0860

Complete contact information is available at: https://pubs.acs.org/10.1021/acs.jpcb.4c04082

Author Contributions

Y.K., A.A., and J.M. planned and designed the research. Y.K. and A.A. generated the samples. Y.K. and D.G. conducted NMR experiments. Y.K. analyzed the NMR data and performed NSD. C.W. performed DFT calculations. Y.K. and J.M. interpreted data and wrote the manuscript. All authors have read and agreed to the published version of the manuscript.

Notes

The authors declare no competing financial interest.

■ ACKNOWLEDGMENTS

The authors thank Dr. Chen Song (University of Leipzig) and Dr. Pavlo Bielytskyi (Bruker BioSpin GmbH) for their valuable discussions on data analysis. The authors acknowledge Dr. Jens Krumsieck (TU Braunschweig) for his helpful advice and discussions regarding *PorphyStruct* analysis. The authors further thank to Prof. Günter Grampp (TU Graz) for helpful discussions on Marcus theory as well as Prof. Wolfgang Gärtner (University of Leipzig) for reading and correcting our manuscript. The authors also acknowledge the members of Prof. Peter W. Hildebrand's group at the University of Leipzig for inspiring discussions as well as Prof. Daniel Huster (University of Leipzig) and Prof. Kay Saalwächter (University of Halle) for their helpful discussions on DIPSHIFT. Furthermore, the authors are deeply grateful to Prof. Wolfgang Lubitz (Max Planck Institute for Chemical Energy Conversion) for his insightful discussion on photosynthetic systems. J.M. and Y.K. gratefully acknowledges the *Deutsche Forschungsgemeinschaft* (DFG, German Research Foundation) through projects MA4972/15-1 and TRR-386 HYP*MOL—A1 and A3 (514664767). C.W. gratefully acknowledges the resources on the LiCCA HPC cluster of the University of Augsburg cofunded by the DFG grant number 499211671.

■ ABBREVIATIONS

ALA:δ-aminolevulinic acid; BChl:bacteriochlorophyll; CIDNP:chemically induced dynamic nuclear polarization; CEST:chemical exchange saturation transfer; CODEX:center-band-only detection of exchange; CSA:chemical shift anisotropy; DARR:dipolar-assisted rotational resonance; DD:differential decay; DFT:density functional theory; DIPSHIFT:dipolar-chemical shift correlation; DR:differential relaxation; NSD:Normal-coordinate Structural Decomposition; ET:electron transfer; EXSY:exchange spectroscopy; fMLF:*N*-formyl-methionyl-leucyl-phenylalanine; HbRCs:heliobacterial reaction centers; *Hb. mobilis*:*Helibacillus mobilis*; *H. modesticaldum*:*Heliobacterium modesticaldum*; MAS:magic-angle spinning; MD:molecular dynamics; NMR:nuclear magnetic resonance; NSD:normal-coordinate structural decomposition; OD:optical density; PAF:principal axes frame; PSII:photosystem II; PRE:paramagnetic relaxation enhancement; PbRCs:puple bacterial reaction centers; RC:reaction center; *R. sphaeroides*:*Rhodobacter sphaeroides*; SCRP:spin correlated radical pair; SUPER:separation of undistorted powder patterns by effortless recoupling; SLF:separated-local field; SW_f-TPPM:sweep-frequency two-pulse phase pulse modulation; TSM:three-spin mixing; WT:wild type

■ REFERENCES

(1) Jones, M. R. Photosynthesis: A New twist to biological solar power. *Curr. Biol.* **1997**, *7*, R541−R543.

(2) Gao, F.; Liu, G.; Chen, A.; Hu, Y.; Wang, H.; Pan, J.; Feng, J.; Zhang, H.; Wang, Y.; Min, Y.; et al. Artificial photosynthetic cells with biotic−abiotic hybrid energy modules for customized CO_2 Conversion. *Nat. Commun.* **2023**, *14*, No. 6783.

(3) Berhanu, S.; Ueda, T.; Kuruma, Y. Artificial photosynthetic cell producing energy for protein synthesis. *Nat. Commun.* **2019**, *10*, No. 1325.

(4) Scheer, H. Chlorophylls: A Personal Snapshot. *Molecules* **2022**, *27*, 1093.

(5) Lin, S.; Chiou, H. C.; Kleinherenbrink, F. A.; Blankenship, R. E. Time-resolved spectroscopy of energy and electron transfer processes in the photosynthetic bacterium *heliobacillus mobilis*. *Biophys. J.* **1994**, *66*, 437−445.

(6) Holzwarth, A. R.; Müller, M. G.; Reus, M.; Nowaczyk, M.; Sander, J.; Rögner, M. Kinetics and mechanism of electron transfer in intact photosystem II and in the isolated reaction center: Pheophytin is the primary electron acceptor. *Proc. Natl. Acad. Sci. U.S.A.* **2006**, *103*, 6895−6900.

(7) Berera, R.; van Grondelle, R.; Kennis, J. T. M. Ultrafast transient absorption spectroscopy: principles and application to photosynthetic systems. *Photosynth. Res.* **2009**, *101*, 105−118.

(8) Di Donato, M.; Groot, M. L. Ultrafast infrared spectroscopy in photosynthesis. *Biochim. Biophys. Acta, Bioenerg.* **2015**, *1847*, 2−11.

(9) Nesterov, A. I.; Berman, G. P. Role of protein fluctuation correlations in electron transfer in photosynthetic complexes. *Phys. Rev. E* **2015**, *91*, No. 24072.

(10) Pudlák, M.; Pincák, R.; Bartoš, E. Effect of vibrational modes on electron transfer directionality: Photosynthetic reaction centers. *Phys. Rev. E* **2022**, *105*, No. 064408.

(11) Poddubnyy, V. V.; Glebov, I. O.; Eremin, V. V. Protein vibration effects on primary electron transfer dynamics in *Rhodobacter sphaeroides* photosynthetic reaction center. *J. Phys. Chem. B* **2017**, *121*, 10639−10647.

(12) Stowell, M. H. B.; McPhillips, T. M.; Rees, D. C.; Soltis, S. M.; Abresch, E.; Feher, G. Light-induced structural changes in photosynthetic reaction center: Implications for mechanism of electron-proton transfer. *Science* **1997**, *276*, 812−816.

(13) Wöhri, A. B.; Katona, G.; Johansson, L. C.; Fritz, E.; Malmerberg, E.; Andersson, M.; Vincent, J.; Eklund, M.; Cammarata, M.; Wulff, M.; et al. Light-induced structural changes in a photosynthetic reaction center caught by laue diffraction. *Science* **2010**, *328*, 630−633.

(14) Nonella, M.; Schulten, K. Molecular dynamics simulation of electron transfer in proteins: Theory and application to $Q_A \rightarrow Q_B$ transfer in the photosynthetic reaction center. *J. Phys. Chem. A* **1991**, *95*, 2059−2067.

(15) Milanovsky, G. E.; Ptushenko, V. V.; Golbeck, J. H.; Semenov, A. Y.; Cherepanov, D. A. Molecular dynamics study of the primary charge separation reactions in photosystem I: effect of the replacement of the axial ligands to the electron acceptor A_0. *Biochim. Biophys. Acta, Bioenerg.* **2014**, *1837*, 1472−1483.

(16) Vasil'ev, S.; Bruce, D. A protein dynamics study of photosystem II: The effects of protein conformation on reaction center function. *Biophys. J.* **2006**, *90*, 3062−3073.

(17) Xu, D.; Schulten, K. Coupling of protein motion to electron transfer in a photosynthetic reaction center: Investigating the low temperature behavior in the framework of the spin-boson model. *Chem. Phys.* **1994**, *182*, 91−117.

(18) Parson, W. W.; Chu, Z. T.; Warshel, A. Electrostatic control of charge separation in bacterial photosynthesis. *Biochim. Biophys. Acta, Bioenerg.* **1990**, *1017*, 251−272.

(19) Marcus, R. A. Electron transfer reactions in chemistry: Theory and experiment (Nobel Lecture). *Angew. Chem., Int. Ed.* **1993**, *32*, 1111−1121.

(20) Marcus, R. A.; Sutin, N. Electron transfers in chemistry and biology. *Biochim. Biophys. Acta, Rev. Bioenerg.* **1985**, *811*, 265−322.

(21) Senge, M. O.; MacGowan, S. A.61 The structural chemistry of isolated chlorophylls. In *Handbook of Porphyrin Science*; World Scientific Publishing Company, 2010; Vol. *13*, pp 253−297 DOI: 10.1142/9789814322386_0013.

(22) Jentzen, W.; Ma, J. G.; Shelnutt, J. A. Conservation of the conformation of the porphyrin macrocycle in hemoproteins. *Biophys. J.* **1998**, *74*, 753−763.

(23) Geno, M. K.; Halpern, J. Why does nature not use the porphyrin ligand in vitamin B12? *J. Am. Chem. Soc.* **1987**, *109*, 1238−1240.

(24) Olea, C.; Kuriyan, J.; Marletta, M. A. Modulating heme redox potential through protein-induced porphyrin distortion. *J. Am. Chem. Soc.* **2010**, *132*, 12794−12795.

(25) Imada, Y.; Nakamura, H.; Takano, Y. Density functional study of porphyrin distortion effects on redox potential of heme. *J. Comput. Chem.* **2018**, *39*, 143−150.

(26) Cardona, T. Thinking twice about the evolution of photosynthesis. *Open Biol.* **2019**, *9*, No. 180246.

(27) Blankenship, R. E. Early evolution of photosynthesis. *Plant Physiol.* **2010**, *154*, 434−438.

(28) Orf, G. S.; Gisriel, C.; Redding, K. E. Evolution of photosynthetic reaction centers: Insights from the structure of the heliobacterial reaction center. *Photosynth. Res.* **2018**, *138*, 11−37.

(29) Liebl, U.; Mockensturm-Wilson, M.; Trost, J. T.; Brune, D. C.; Blankenship, R. E.; Vermaas, W. Single core polypeptide in the reaction center of the photosynthetic bacterium heliobacillus mobilis: Structural implications and relations to other photosystems. *Proc. Natl. Acad. Sci. U.S.A.* **1993**, *90*, 7124−7128.

(30) Gisriel, C.; Sarrou, I.; Ferlez, B.; Golbeck, J. H.; Redding, K. E.; Fromme, R. Structure of a symmetric photosynthetic reaction center-photosystem. *Science* **2017**, *357*, 1021−1025.

(31) Kaur, D.; Ferlez, B.; Landry, P.; Biskup, T.; Weber, S.; Golbeck, J. H.; Lakshmi, K. V.; van der Est, A. Electronic structure and energetics of a heterodimeric BChl g'/Chl a' special pair generated by exposure of *Heliomicrobium modesticaldum* to dioxygen. *Phys. Chem. Chem. Phys.* **2023**, *25*, 26894−26905.

(32) Frolov, D.; Wakeham, M. C.; Andrizhiyevskaya, E. G.; Jones, M. R.; Van Grondelle, R. Investigation of B-branch electron transfer by femtosecond time resolved spectroscopy in a *Rhodobacter sphaeroides* reaction centre that lacks the Q_A ubiquinone. *Biochim. Biophys. Acta, Bioenerg.* **2005**, *1707*, 189−198.

(33) Kolbasov, D.; Scherz, A. Asymmetric electron transfer in reaction centers of purple bacteria strongly depends on different electron matrix

https://doi.org/10.1021/acs.jpcb.4c04082
J. Phys. Chem. B 2024, 128, 11525−11545

elements in the active and inactive branches. *J. Phys. Chem. B* **2000**, *104*, 1802−1809.
(34) McDowell, L. M.; Kirmaier, C.; Holten, D.; Gaul, D.; Schenck, C. C. Investigation into the source of electron transfer asymmetry in bacterial reaction centers. *Biochemistry* **1991**, *30*, 8315−8322.
(35) Oh-oka, H. Type 1 reaction center of photosynthetic heliobacteria. *Photochem. Photobiol.* **2007**, *83*, 177−186.
(36) Jeschke, G. Electron-electron-nuclear three-spin mixing in spin-correlated radical pairs. *J. Chem. Phys.* **1997**, *106*, 10072−10086.
(37) Mcdermott, A.; Zysmilich, M. G.; Polenová, T. Solid State NMR Studies of Photoinduced Polarization in Photosynthetic Reaction Centers: Mechanism and Simulations. *Solid State Nucl. Magn. Reson.* **1998**, *11*, 21−47.
(38) Polenova, T.; McDermott, A. E. A Coherent mixing mechanism explains the photoinduced nuclear polarization in photosynthetic reaction centers. *J. Phys. Chem. B* **1999**, *103*, 535−548.
(39) Kleinherenbrink, F. A. M.; Ikegami, I.; Hiraishi, A.; Otte, S. C. M.; Amesz, J. Electron transfer in menaquinone-depleted membranes of *Heliobacterium chlorum*. *Biochim. Biophys. Acta, Bioenerg.* **1993**, *1142*, 69−73.
(40) Ferlez, B.; Cowgill, J.; Dong, W.; Gisriel, C.; Lin, S.; Flores, M.; Walters, K.; Cetnar, D.; Redding, K. E.; Golbeck, J. H. Thermodynamics of the electron acceptors in *Heliobacterium modesticaldum*: An exemplar of an early homodimeric type i photosynthetic reaction center. *Biochemistry* **2016**, *55*, 2358−2370.
(41) Kleinherenbrink, F. A. M.; Aartsma, T. J.; Amesz, J. Charge separation and formation of bacteriochlorophyll triplets in *Heliobacterium chlorum*. *Biochim. Biophys. Acta, Bioenerg.* **1991**, *1057*, 346−352.
(42) Smit, H. W. J.; Amesz, J.; van der Hoeven, M. F. R. Electron transport and triplet formation in membranes of the photosynthetic bacterium *Heliobacterium chlorum*. *Biochim. Biophys. Acta, Bioenerg.* **1987**, *893*, 232−240.
(43) Ferlez, B.; Agostini, A.; Carbonera, D.; Golbeck, J. H.; Van Der Est, A. Triplet charge recombination in heliobacterial reaction centers does not produce a spin-polarized EPR spectrum. *Z. Phys. Chem.* **2017**, *231*, 593−607.
(44) Thamarath, S. S.; Alia, A.; Daviso, E.; Mance, D.; Golbeck, J. H.; Matysik, J. Whole cell nuclear magnetic resonance characterization of two photochemically active states of the photosynthetic reaction center in heliobacteria. *Biochemistry* **2012**, *51*, 5763−5773.
(45) Surendran Thamarath, S.; Alia, A.; Roy, E.; Sai Sankar Gupta, K. B.; Golbeck, J. H.; Matysik, J. The field-dependence of the solid-state photo-CIDNP effect in two states of heliobacterial reaction centers. *Photosynth. Res.* **2013**, *117*, 461−469.
(46) Schenck, C. C.; Parson, W. W.; Holten, D.; Windsor, M. W.; Sarai, A. Temperature dependence of electron transfer between bacteriopheophytin and ubiquinone in protonated and deuterated reaction centers of *Rhodopseudomonas sphaeroides*. *Biophys. J.* **1981**, *36*, 479−489.
(47) Prakash, S.; Alia; Gast, P.; De Groot, H. J. M.; Jeschke, G.; Matysik, J. Magnetic field dependence of photo-CIDNP MAS NMR on photosynthetic reaction centers of *Rhodobacter sphaeroides* WT. *J. Am. Chem. Soc.* **2005**, *127*, 14290−14298.
(48) Matysik, J.; Diller, A.; Roy, E.; Alia, A. The solid-state photo-CIDNP effect. *Photosynth. Res.* **2009**, *102*, 427−435.
(49) Daviso, E.; Alia, A.; Prakash, S.; Diller, A.; Gast, P.; Lugtenburg, J.; Matysik, J.; Jeschke, G. Electron-nuclear spin dynamics in a bacterial photosynthetic reaction center. *J. Phys. Chem. C* **2009**, *113*, 10269−10278.
(50) Matysik, J.; Ding, Y.; Kim, Y.; Kurle, P.; Yurkovskaya, A.; Ivanov, K.; Alia, A. Photo-CIDNP in solid state. *Appl. Magn. Reson.* **2022**, *53*, 521−537.
(51) Sai Sankar Gupta, K. B.; Alia, A.; De Groot, H. J. M.; Matysik, J. Symmetry break of special pair: Photochemically induced dynamic nuclear polarization NMR confirms control by nonaromatic substituents. *J. Am. Chem. Soc.* **2013**, *135*, 10382−10387.
(52) Prakash, S.; Alia; Gast, P.; De Groot, H. J. M.; Matysik, J.; Jeschke, G. Photo-CIDNP MAS NMR in intact cells of *Rhodobacter sphaeroides* R26: Molecular and atomic resolution at nanomolar concentration. *J. Am. Chem. Soc.* **2006**, *128*, 12794−12799.
(53) Janssen, G. J.; Roy, E.; Matysik, J.; Alia, A. ^{15}N photo-CIDNP MAS NMR to reveal functional heterogeneity in electron donor of different plant organisms. *Appl. Magn. Reson.* **2012**, *42*, 57−67.
(54) Janssen, G. J.; Eschenbach, P.; Kurle, P.; Bode, B. E.; Neugebauer, J.; de Groot, H. J. M.; Matysik, J.; Alia, A. Analysis of the electronic structure of the primary electron donor of photosystem I of *Spirodela oligorrhiza* by photochemically induced dynamic nuclear polarization (Photo-CIDNP) solid-state nuclear magnetic resonance (NMR). *Magn. Reson.* **2020**, *1*, 261−274.
(55) Thamarath, S. S.; Heberle, J.; Hore, P. J.; Kottke, T.; Matysik, J. Solid-state photo-CIDNP effect observed in phototropin LOV1-C57S by ^{13}C magic-angle spinning NMR spectroscopy. *J. Am. Chem. Soc.* **2010**, *132*, 15542−15543.
(56) Ding, Y.; Kiryutin, A. S.; Yurkovskaya, A. V.; Sosnovsky, D. V.; Sagdeev, R. Z.; Bannister, S.; Kottke, T.; Kar, R. K.; Schapiro, I.; Ivanov, K. L.; Matysik, J. Nuclear spin-hyperpolarization generated in a flavoprotein under illumination: experimental field-dependence and theoretical level crossing analysis. *Sci. Rep.* **2019**, *9*, No. 18436.
(57) Ding, Y.; Kiryutin, A. S.; Zhao, Z.; Xu, Q. Z.; Zhao, K. H.; Kurle, P.; Bannister, S.; Kottke, T.; Sagdeev, R. Z.; Ivanov, K. L.; et al. Tailored flavoproteins acting as light-driven spin machines pump nuclear hyperpolarization. *Sci. Rep.* **2020**, *10*, No. 18658.
(58) Richter, G.; Weber, S.; Römisch, W.; Bacher, A.; Fischer, M.; Eisenreich, W. Photochemically induced dynamic nuclear polarization in a C450A mutant of the LOV2 domain of the *avena sativa* blue-light receptor phototropin. *J. Am. Chem. Soc.* **2005**, *127*, 17245−17252.
(59) Schanda, P.; Ernst, M. Studying dynamics by magic-angle spinning solid-state NMR spectroscopy: Principles and applications to biomolecules. *Prog. Nucl. Magn. Reson. Spectrosc.* **2016**, *96*, 1−46.
(60) Krushelnitsky, A.; Reichert, D. Solid-state NMR and protein dynamics. *Prog. Nucl. Magn. Reson. Spectrosc.* **2005**, *47*, 1−25.
(61) Palmer, A. G. Chemical exchange in biomacromolecules: Past, rresent, and future. *J. Magn. Reson.* **2014**, *241*, 3−17.
(62) Vallurupalli, P.; Bouvignies, G.; Kay, L. E. Studying "Invisible" excited protein states in slow exchange with a major state conformation. *J. Am. Chem. Soc.* **2012**, *134*, 8148−8161.
(63) Krushelnitsky, A.; DeAzevedo, E.; Linser, R.; Reif, B.; Saalwächter, K.; Reichert, D. Direct observation of millisecond to second motions in proteins by dipolar CODEX NMR spectroscopy. *J. Am. Chem. Soc.* **2009**, *131*, 12097−12099.
(64) Tycko, R.; Dabbagh, G.; Mirau, P. A. Determination of chemical-shift-anisotropy lineshapes in a two-dimensional magic-angle-spinning NMR experiment. *J. Magn. Reson.* **1989**, *85*, 265−274.
(65) Meirovitch, E.; Liang, Z.; Freed, J. H. Protein dynamics in the solid state from 2H NMR line shape analysis: A consistent perspective. *J. Phys. Chem. B* **2015**, *119*, 2857−2868.
(66) Hester, R. K.; Ackerman, J. L.; Neff, B. L.; Waugh, J. S. Separated local field spectra in NMR: Determination of structure of solids. *Phys. Rev. Lett.* **1976**, *36*, 1081−1083.
(67) Cobo, M. F.; Achilles, A.; Reichert, D.; Deazevedo, E. R.; Saalwächter, K. Recoupled separated-local-field experiments and applications to study intermediate-regime molecular motions. *J. Magn. Reson.* **2012**, *221*, 85−96.
(68) Munowitz, M. G.; Griffin, R. G.; Bodenhausen, G.; Huang, T. H. Two-dimensional rotational spin-echo nuclear magnetic resonance in solids: Correlation of chemical shift and dipolar interactions. *J. Am. Chem. Soc.* **1981**, *103*, 2529−2533.
(69) DeAzevedo, E. R.; Saalwachter, K.; Pascui, O.; De Souza, A. A.; Bonagamba, T. J.; Reichert, D. Intermediate motions as studied by solid-state separated local field NMR experiments. *J. Chem. Phys.* **2008**, *128*, No. 104505.
(70) Krushelnitsky, A.; Reichert, D.; Saalwächter, K. Solid-state NMR approaches to internal dynamics of proteins: From picoseconds to microseconds and seconds. *Acc. Chem. Res.* **2013**, *46*, 2028−2036.
(71) Zinkevich, T.; Chevelkov, V.; Reif, B.; Saalwächter, K.; Krushelnitsky, A. Internal protein dynamics on ps to μs timescales as

https://doi.org/10.1021/acs.jpcb.4c04082
J. Phys. Chem. B 2024, 128, 11525−11545

studied by multi-frequency ^{15}N solid-state NMR relaxation. *J. Biomol. NMR* **2013**, *57*, 219−235.
(72) Chevelkov, V.; Diehl, A.; Reif, B. Measurement of ^{15}N - T_1 relaxation rates in a perdeuterated protein by magic angle spinning solid-state nuclear magnetic resonance spectroscopy. *J. Chem. Phys.* **2008**, *128*, 052316.
(73) Matysik, J.; Kim, Y.; Kurle-Tucholski, P.; Musabirova, G.; Qin, R.; Alia, A. Structural elucidation based on photo-CIDNP NMR. In *Integrated Structural Biology*; Polenova, T.; Gronenborn, A.; Quinn, C., Eds.; Royal Society of Chemistry: London, UK, 2023; Vol. *30*, pp 301−326.
(74) van de Meent, E. J.; Kleinherenbrink, F. A. M.; Amesz, J. Purification and properties of an antenna-reaction center complex from heliobacteria. *Biochim. Biophys. Acta, Bioenerg.* **1990**, *1015*, 223−230.
(75) Kim, Y.; Alia, A.; Kurle-Tucholski, P.; Wiebeler, C.; Matysik, J. Electronic structures of radical - pair - forming cofactors in a heliobacterial reaction center. *Molecules* **2024**, *29*, 1021.
(76) Bielytskyi, P.; Gräsing, D.; Zahn, S.; Mote, K. R.; Alia, A.; Madhu, P. K.; Matysik, J. Assignment of NMR resonances of potons covalently bound to photochemically active cofactors in photosynthetic reaction centers by ^{13}C−^{1}H Photo-CIDNP MAS-J-HMQC experiment. *J. Magn. Reson.* **2019**, *298*, 64−76.
(77) Sai Sankar Gupta, K. B.; Alia, A.; Buda, F.; De Groot, H. J. M.; Matysik, J. Bacteriopheophytin a in the active branch of the reaction center of *Rhodobacter Sphaeroides* is not disturbed by the protein matrix as shown by ^{13}C photo-CIDNP MAS NMR. *J. Phys. Chem. B* **2013**, *117*, 3287−3297.
(78) Shochat, S.; Arlt, T.; Francke, C.; Gast, P.; van Noort, P. I.; Otte, S. C. M.; Schelvis, H. P. M.; Schmidt, S.; Vijgenboom, E.; Vrieze, J.; et al. A. J. Spectroscopic characterization of reaction centers of the (M)Y210W mutant of the photosynthetic bacterium *Rhodobacter sphaeroides*. *Photosynth. Res.* **1994**, *40*, 55−66.
(79) Okamura, M. Y.; Isaacson, R. A.; Feher, G. Primary acceptor in bacterial photosynthesis: obligatory role of ubiquinone in photoactive reaction centers of *Rhodopseudomonas spheroides*. *Proc. Natl. Acad. Sci. U.S.A.* **1975**, *72*, 3491−3495.
(80) Neue, G.; Dybowski, C. Determining temperature in magic-angle spinning probe using the temperature dependence of the isotropic chemical shift of lead nitrate. *Solid State Nucl. Magn. Reson.* **1997**, *7*, 333−336.
(81) Concistrè, M.; Gansmüller, A.; McLean, N.; Johannessen, O. G.; Marín Montesinos, I.; Bovee-Geurts, P. H. M.; Verdegem, P.; Lugtenburg, J.; Brown, R. C. D.; DeGrip, W. J.; Levitt, M. H. Double-quantum ^{13}C nuclear magnetic resonance of bathorhodopsin, the first photointermediate in mammalian vision. *J. Am. Chem. Soc.* **2008**, *130*, 10490−10491.
(82) Huster, D. Investigations of the structure and dynamics of membrane-associated peptides by magic angle spinning NMR. *Prog. Nucl. Magn. Reson. Spectrosc.* **2005**, *46*, 79−107.
(83) Fowler, D. J.; Harris, M. J.; Thompson, L. K. Heat management strategies for solid-state NMR of functional proteins. *J. Magn. Reson.* **2012**, *222*, 112−118.
(84) Thakur, R. S.; Kurur, N. D.; Madhu, P. K. Swept-frequency two-pulse phase modulation for heteronuclear dipolar decoupling in solid-state NMR. *Chem. Phys. Lett.* **2006**, *426*, 459−463.
(85) Ivanir-Dabora, H.; Nimerovsky, E.; Madhu, P. K.; Goldbourt, A. Site-resolved backbone and side-chain intermediate dynamics in a carbohydrate-binding module protein studied by magic-angle spinning NMR spectroscopy. *Chem. − Eur. J.* **2015**, *21*, 10778−10785.
(86) Vinogradov, E.; Madhu, P. K.; Vega, S. Phase modulated lee-goldburg magic angle spinning proton nuclear magnetic resonance experiments in the solid state: A bimodal floquet theoretical treatment. *J. Chem. Phys.* **2001**, *115*, 8983−9000.
(87) Bak, M.; Rasmussen, J. T.; Nielsen, N. C. SIMPSON: A general simulation program for solid-state NMR spectroscopy. *J. Magn. Reson.* **2000**, *147*, 296−330.
(88) Destro, R.; Marsh, R. E.; Bianchi, R. A Low-Temperature (23 K) Study of L-Alanine. *J. Phys. Chem. A* **1988**, *92* (4), 966−973.
(89) Liu, S. F.; Mao, J. D.; Schmidt-Rohr, K. A Robust technique for two-dimensional separation of undistorted chemical-shift anisotropy powder patterns in magic-angle-spinning NMR. *J. Magn. Reson.* **2002**, *155*, 15−28.
(90) Gräsing, D.; Dziubińska-Kühn, K. M.; Zahn, S.; Alia, A.; Matysik, J. Studying Hydrogen Bonding and Dynamics of the Acetylate Groups of the Special Pair of *Rhodobacter sphaeroides* WT. *Sci. Rep.* **2019**, *9*, No. 10528.
(91) Marion, D.; Wüthrich, K. Application of phase sensitive two-dimensional correlated spectroscopy (COSY) for measurements of ^{1}H−^{1}H spin−spin coupling constants in proteins. *Biochem. Biophys. Res. Commun.* **1983**, *113*, 967−974.
(92) Takegoshi, K. Homonuclear shift-correlation experiment in solids. In *Modern Magnetic Resonance*; Webb, G. A., Ed.; Springer: Dordrecht, The Netherlands, 2008; pp 689−693.
(93) Takegoshi, K.; Nakamura, S.; Terao, T. ^{13}C-^{1}H Dipolar-driven ^{13}C-^{13}C recoupling without ^{13}C RF irradiation in nuclear magnetic resonance of rotating solids. *J. Chem. Phys.* **2003**, *118*, 2325−2341.
(94) Hanwell, M. D.; Curtis, D. E.; Lonie, D. C.; Vandermeersch, T.; Zurek, E.; Hutchison, G. R. Avogadro: An advanced semantic chemical editor, visualization, and analysis platform. *J. Cheminform.* **2012**, *4*, 1−17.
(95) Neese, F. Software Update: The ORCA Program System—Version 5.0. *Wiley Interdiscip. Rev.: Comput. Mol. Sci.* **2022**, *12*, 1−15.
(96) Grimme, S.; Brandenburg, J. G.; Bannwarth, C.; Hansen, A. Consistent structures and interactions by density functional theory with small atomic orbital basis sets. *J. Chem. Phys.* **2015**, *143*, No. 054107.
(97) Krumsieck, J.; Bröring, M. PorphyStruct : A digital tool for the quantitative assignment of non-planar distortion modes in four-membered porphyrinoids. *Chem. — Eur. J.* **2021**, *27*, 11580−11588.
(98) Jentzen, W.; Song, X. Z.; Shelnutt, J. A. Structural characterization of synthetic and protein-bound porphyrins in terms of the lowest-frequency normal coordinates of the macrocycle. *J. Phys. Chem. B* **1997**, *101*, 1684−1699.
(99) Najdanova, M.; Gräsing, D.; Alia, A.; Matysik, J. Analysis of the electronic structure of the special pair of a bacterial photosynthetic reaction center by ^{13}C photochemically induced dynamic nuclear polarization magic-angle spinning NMR using a double-quantum axis. *Photochem. Photobiol.* **2018**, *94*, 69−80.
(100) Thamarath, S. S.; Bode, B. E.; Prakash, S.; Sai Sankar Gupta, K. B.; Alia, A.; Jeschke, G.; Matysik, J. Electron spin density distribution in the special pair triplet of *Rhodobacter sphaeroides* R26 revealed by magnetic field dependence of the solid-state photo-CIDNP effect. *J. Am. Chem. Soc.* **2012**, *134*, 5921−5930.
(101) Siemer, A. B.; Huang, K. Y.; McDermott, A. E. Protein linewidth and solvent dynamics in frozen solution NMR. *PLoS One* **2012**, *7*, No. e47242.
(102) Fiedor, L.; Kania, A.; Myśliwa-Kurdziel, B.; Orzeł, Ł.; Stochel, G. Understanding chlorophylls: Central magnesium ion and phytyl as structural determinants. *Biochim. Biophys. Acta, Bioenerg.* **2008**, *1777*, 1491−1500.
(103) Gorka, M.; Baldansuren, A.; Malnati, A.; Gruszecki, E.; Golbeck, J. H.; Lakshmi, K. V. Shedding light on primary donors in photosynthetic reaction centers. *Front. Microbiol.* **2021**, *12*, No. 735666.
(104) Lauterwasser, C.; Finkele, U.; Scheer, H.; Zinth, W. Temperature dependence of the primary electron transfer in photosynthetic reaction centers from *Rhodobacter sphaeroides*. *Chem. Phys. Lett.* **1991**, *183*, 471−477.
(105) Miyamoto, R.; Iwaki, M.; Mino, H.; Harada, J.; Itoh, S.; Oh-Oka, H. ESR signal of the iron-sulfur center F_X and its function in the homodimeric reaction center of *Heliobacterium modesticaldum*. *Biochemistry* **2006**, *45*, 6306−6316.
(106) Ringe, D.; Petsko, G. A. The "glass transition" in protein dynamics: What it is, why it occurs, and how to exploit it. *Biophys. Chem.* **2003**, *105*, 667−680.
(107) Brownsey, G. J.; Noel, T. R.; Parker, R.; Ring, S. G. The Glass Transition behavior of the globular protein bovine serum albumin. *Biophys. J.* **2003**, *85*, 3943−3950.

(108) Kim, C. U.; Tate, M. W.; Gruner, S. M. Protein dynamical transition at 110 K. *Proc. Natl. Acad. Sci. U.S.A.* **2011**, *108*, 20897−20901.
(109) Schnegg, A.; Fuhs, M.; Rohrer, M.; Lubitz, W.; Prisner, T. F.; Möbius, K. Molecular dynamics of $Q_A^{-\bullet}$ and $Q_B^{-\bullet}$ in photosynthetic bacterial reaction centers studied by pulsed high-field EPR at 95 GHz. *J. Phys. Chem. B* **2002**, *106*, 9454−9462.
(110) Marion, D.; Gauto, D. F.; Ayala, I.; Giandoreggio-Barranco, K.; Schanda, P. Microsecond protein dynamics from combined bloch-mcConnell and near-rotary-resonance $R_{1\rho}$ relaxation-dispersion MAS NMR. *ChemPhysChem* **2019**, *20*, 276−284.
(111) Kraus, J.; Gupta, R.; Lu, M.; Gronenborn, A. M.; Akke, M.; Polenova, T. Accurate backbone ^{13}C and ^{15}N chemical shift tensors in galectin-3 determined by MAS NMR and QM/MM: Details of structure and environment matter. *ChemPhysChem* **2020**, *21*, 1436−1443.
(112) Köhler, L.; Gärtner, W.; Salvan, G.; Matysik, J.; Wiebeler, C.; Song, C. Photocycle of a cyanobacteriochrome: A charge defect on ring C impairs conjugation in chromophore. *Chem. Sci.* **2023**, *14*, 6295−6308.
(113) Schmidt-Rohr, K.; Spiess, H. W. *Multidimensional Solid-State NMR and Polymers*; Academic Press: London, UK, 1994; Vol. *XVIII*, pp 28−39.
(114) Schanda, P. Relaxing with liquids and solids − A perspective on biomolecular dynamics. *J. Magn. Reson.* **2019**, *306*, 180−186.
(115) Jagannathan, B.; Golbeck, J. H. Fx, Fa, and Fb iron-sulfur clusters in type I photosynthetic reaction centers. In *Encyclopedia of Biological Chemistry*, 2nd ed.; Lennarz, W. J.; Lane, M. D., Eds.; Elsevier Inc.: Amsterdam, The Netherlands, 2013; pp 335−342.
(116) Furman, G. B.; Goren, S. D. Spin diffusion and spin-lattice relaxation in pulse spin-locking in solids containing paramagnetic impurities. *J. Phys.: Condens. Matter* **1999**, *11*, 8275−8282.
(117) Mark Henrichs, P.; Cofield, M. L.; Young, R. H.; Michael Hewitt, J. Nuclear spin-lattice relaxation via paramagnetic centers in solids. ^{13}C NMR of diamonds. *J. Magn. Reson.* **1984**, *58*, 85−94.
(118) Gottstein, D.; Reckel, S.; Dötsch, V.; Güntert, P. Requirements on paramagnetic relaxation enhancement data for membrane protein structure determination by NMR. *Structure* **2012**, *20*, 1019−1027.
(119) Bloembergen, N. On the interaction of nuclear spins in a crystalline lattice. *Physica* **1949**, *15*, 386−426.
(120) Veshtort, M.; Griffin, R. G. Proton-driven spin diffusion in rotating solids via reversible and irreversible quantum dynamics. *J. Chem. Phys.* **2011**, *135*, No. 134509.
(121) Dumez, J. N. Many body dynamics in nuclear spin diffusion. Doctoral dissertation, Écolenormale supérieure: Lyon, 2011.
(122) Song, C.; Lang, C.; Kopycki, J.; Hughes, J.; Matysik, J. NMR Chemical shift pattern changed by ammonium sulfate precipitation in cyanobacterial phytochrome Cph1. *Front. Mol. Biosci.* **2015**, *2*, 42.
(123) Sai Sankar Gupta, K. B. Spin-torch experiments on reaction centers of Rhodobacter Sphaeroides, Doctoral dissertation, Leiden University: Leiden, 2011.
(124) Röder, B.; Büchner, M.; Rückmann, I.; Senge, M. O. Correlation of photophysical parameters with macrocycle distortion in porphyrins with graded degree of saddle distortion. *Photochem. Photobiol. Sci.* **2010**, *9*, 1152−1158.
(125) MacGowan, S. A.; Senge, M. O. Conformational control of cofactors in nature-functional tetrapyrrole conformations in the photosynthetic reaction centers of purple bacteria. *Chem. Commun.* **2011**, *47*, 11621−11623.
(126) Saito, K.; Umena, Y.; Kawakami, K.; Shen, J. R.; Kamiya, N.; Ishikita, H. Deformation of chlorin rings in the photosystem II crystal structure. *Biochemistry* **2012**, *51*, 4290−4299.
(127) Prince, R. C.; Gest, H.; Blankenship, R. E. Thermodynamic properties of the photochemical reaction center of *Heliobacterium chlorum*. *Biochim. Biophys. Acta, Bioenerg.* **1985**, *810*, 377−384.
(128) Kanda, T.; Ishikita, H. Energetic diversity in the electron-transfer pathways of Type I photosynthetic reaction centers. *Biochemistry* **2023**, *62*, 934−941.
(129) Zhou, Z.; Shen, M.; Cao, C.; Liu, Q.; Yan, Z. Opposing influences of ruffling and doming deformation on the 4-N cavity size of porphyrin macrocycles: The role of heme deformations revealed. *Chem. − Eur. J.* **2012**, *18*, 7675−7679.
(130) Schulten, E. A. M.; Matysik, J.; Alia; Kiihne, S.; Raap, J.; Lugtenburg, J.; Gast, P.; Hoff, A. J.; de Groot, H. J. ^{13}C MAS NMR and photo-CIDNP reveal a pronounced asymmetry in the electronic ground state of the special pair of *Rhodobacter sphaeroides* reaction centers. *Biochemistry* **2002**, *41*, 8708−8717.
(131) Hoff, A. J.; Deisenhofer, J. Photophysics of photosynthesis. Structure and spectroscopy of reaction centers of purple bacteria. *Phys. Rep.* **1997**, *287*, 1−247.
(132) Lendzian, F.; Huber, M.; Isaacson, R. A.; Endeward, B.; Plato, M.; Bönigk, B.; Möbius, K.; Lubitz, W.; Feher, G. The electronic structure of the primary donor cation radical in *Rhodobacter sphaeroides* R-26: ENDOR and TRIPLE resonance studies in single crystals of reaction Centers. *Biochim. Biophys. Acta, Bioenerg.* **1993**, *1183*, 139−160.
(133) Daviso, E.; Prakash, S.; Alia, A.; Gast, P.; Neugebauer, J.; Jeschke, G.; Matysik, J. The electronic structure of the primary electron donor of reaction centers of purple bacteria at atomic resolution as observed by photo-CIDNP ^{13}C NMR. *Proc. Natl. Acad. Sci. U.S.A.* **2009**, *106*, 22281−22286.
(134) Vos, M. H.; Lambry, J. C.; Robles, S. J.; Youvan, D. C.; Breton, J.; Martin, J. L. Direct observation of vibrational coherence in bacterial reaction centers using femtosecond absorption spectroscopy. *Proc. Natl. Acad. Sci. U.S.A.* **1991**, *88*, 8885−8889.
(135) Vos, M. H.; Rappaport, F.; Lambry, J. C.; Breton, J.; Martin, J. L. Visualization of coherent nuclear motion in a membrane protein by femtosecond spectroscopy. *Nature* **1993**, *363*, 320−325.
(136) Yakovlev, A. G.; Shkuropatov, A. Y.; Shuvalov, V. A. Nuclear wavepacket motion producing a reversible charge separation in bacterial reaction centers. *FEBS Lett.* **2000**, *466*, 209−212.
(137) O'Malley, P. J. Density functional predicted geometries and vibrational frequencies of the neutral and anion-radical form of pheophytin: Relevance to electron transfer in photosynthetic reaction centres. *Chem. Phys. Lett.* **2000**, *331*, 78−82.
(138) Müh, F.; Williams, J. A. C.; Allen, J. P.; Lubitz, W. A Conformational change of the photoactive bacteriopheophytin in reaction centers from *Rhodobacter sphaeroides*. *Biochemistry* **1998**, *37*, 13066−13074.
(139) Kothe, G.; Thurnauer, M. C. What you get out of high-time resolution electron paramagnetic resonance: Example from photosynthetic bacteria. *Photosynth. Res.* **2009**, *102*, 349−365.
(140) Heinen, U.; Utschig, L. M.; Poluektov, O. G.; Link, G.; Ohmes, E.; Kothe, G. Structure of the charge separated state $P_{865}^{+}Q_A^{-}$ in the photosynthetic reaction centers of *Rhodobacter Sphaeroides* by quantum beat oscillations and high-field electron paramagnetic resonance: Evidence for light-induced Q_A^{-} reorientation. *J. Am, Chem. Soc.* **2007**, *129*, 15935−15946.
(141) Kleinfeld, D.; Okamura, M. Y.; Feher, G. Electron-transfer kinetics in photosynthetic reaction centers cooled to cryogenic temperatures in the charge-separated state. *Biochemistry* **1984**, *23*, 5780−5786.
(142) Graige, M. S.; Feher, G.; Okamura, M. Y. Conformational gating of the electron transfer reaction $Q_A^{-\bullet}Q_B \rightarrow Q_AQ_B^{-\bullet}$ in bacterial reaction centers of *Rhodobacter sphaeroides* determined by a driving force assay. *Proc. Natl. Acad. Sci. U.S.A.* **1998**, *95*, 11679−11684.
(143) Camara-Artigas, A.; Brune, D.; Allen, J. P. Interactions between lipids and bacterial reaction centers determined by protein crystallography. *Proc. Natl. Acad. Sci. U.S.A.* **2002**, *99*, 11055−11060.
(144) Allen, J. P.; Artz, K.; Lin, X.; Williams, J. C.; Ivancich, A.; Albouy, D.; Mattioli, T. A.; Fetsch, A.; Kuhn, M.; Lubitz, W. Effects of hydrogen bonding to a bacteriochlorophyll-bacteriopheophytin dimer in reaction centers from *Rhodobacter Sphaeroides*. *Biochemistry* **1996**, *35*, 6612−6619.
(145) Lin, X.; Murchison, H. A.; Nagarajan, V.; Parson, W. W.; Allen, J. P.; Williams, J. C. Specific alteration of the oxidation potential of the

https://doi.org/10.1021/acs.jpcb.4c04082
J. Phys. Chem. B 2024, 128, 11525−11545

electron donor in reaction centers from *Rhodobacter sphaeroides*. *Proc. Natl. Acad. Sci. U.S.A.* **1994**, *91*, 10265−10269.
(146) Spiedel, D.; Jones, M. R.; Robert, B. Tuning of the redox potential of the primary electron eonor in reaction centres of purple bacteria: effects of amino acid polarity and position. *FEBS Lett.* **2002**, *527*, 171−175.

NOTE ADDED AFTER ASAP PUBLICATION

This paper published November 8, 2024, with poor quality figures. The corrected version was reposted November 14, 2024.

https://doi.org/10.1021/acs.jpcb.4c04082
J. Phys. Chem. B 2024, 128, 11525−11545